IEEE Access
Multidisciplinary | Rapid Review | Open Access Journal

Received 31 August 2022, accepted 15 September 2022, date of publication 19 September 2022,
date of current version 28 September 2022.

Digital Object Identifier 10.1109/ACCESS.2022.3207746

RESEARCH ARTICLE

Accurate Formulation of the Skin and Proximity Effects in High-Speed Cable System

OUSSAMA GASSAB[1], (Member, IEEE), YANNING CHEN[2], YALI SHAO[2], JINGXIAO LI[1], DING-E WEN[3], FANG HE[4], (Senior Member, IEEE), ZHIZHEN SU[1], PEINA ZHONG[5], JIAN WANG[6], (Member, IEEE), DONGYAN ZHAO[2], (Member, IEEE), AND WEN-YAN YIN[1], (Fellow, IEEE)

[1]College of Information and Electronic Engineering, Innovative Institute of Electromagnetic Information and Electronic Engineering, Zhejiang University, Hangzhou 310058, China
[2]Beijing Smart-Chip Microelectronics Technology Company Ltd.1, Beijing 100192, China
[3]Science and Technology on Electromagnetic Compatibility Laboratory, Wuhan 430064, China
[4]Research and Development Laboratory, Zhejiang Zhaolong Interconnect Technology Company Ltd., Huzhou 313200, China
[5]Hangzhou Applied Acoustics Research Institute, Hangzhou 310022, China
[6]Faculty of Electrical Engineering and Computer Science, Ningbo University, Ningbo 315211, China

Corresponding authors: Oussama Gassab (gassab@zju.edu.cn), Dongyan Zhao (dongyan-zhao@sgchip.sgcc.com.cn), and Wen-Yan Yin (wyyin@zju.edu.cn).

This work was supported in part by the Research and Development Project of Beijing Smart-Chip Microelectronics Technology Company Ltd.1, Zhejiang Provincial Natural Science Foundation of China, under Grant LQ22F010010; and in part by the Natural Science Foundation of China (NSFC) under Grant 62150410440, Grant 61431014, Grant 61931007, Grant 61822112, and Grant 92066105.

ABSTRACT An efficient transmission line model of high-speed cables is established, to predict its response at a high-frequency region (up to 20 GHz). Especially, an appropriate conformal mapping technique is applied to formulate the per-unit-length parameters of high-speed cables. Moreover, the skin and proximity effects of the conducting wires and the outer shield are derived in the closed form. As a result, the AC resistance/ inductance of all the conducting materials due to the skin and proximity effects are accurately incorporated for both layered and unlayered conductors. Furthermore, the mixed-mode S-parameters are precisely predicted for both balanced and unbalanced transmission line cables in the high-frequency region. In addition, the effects of the nonuniformities and cable geometry deformation on the mode conversions are also investigated. The proposed model is firstly validated with commercial software tools, COMSOL, FEKO, and HFSS; then, we further performed physical measurements to verify our new algorithm.

INDEX TERMS High-speed cable, transmission line model, mixed-mode S-parameters, common-mode (CM), differential-mode (DM), shielding, fixtures, skin effect, proximity effect.

I. INTRODUCTION

The first Ethernet network was developed by Xerox in the late of 1970s, and the coaxial cable was used as the transmission medium, in which the transfer rate was only about 3 Mbps. After that, the standardization of the Ethernet was released by the Digital Equipment Corporation (DEC), i.e., Intel and Xerox, in 1979. Thereafter, in 1980 DIX standard named as ''thick Ethernet'' was released. The speed rate of the thick Ethernet was considered to be 10 Mbps, in which the thick coaxial cable was utilized. After that, this standard was revised by the Institute of Electrical and Electronics Engineers (IEEE) in 1983. Hence, the first IEEE standard, which has the name IEEE 802.3, was released [1], and the thick coaxial cable was standardized as 10BASE5. Due to the limitations of the thick coaxial cable, the twisted-wire pair (TWP) Ethernet was applied and standardized as 10BASE-T, then 10BASE-CX was released for shielded TWP cables [2]. In the 1990s, the speed rate increased, and the Gigabit Ethernet was developed, where the shielded copper was used and called 1000BASE-CX and 10GBASE-CX for the speed rate 1 Gbps and 10 Gbps, respectively [3], [4]. Moreover, the development of digital technology requires high-speed data rates in order to transfer data reliably and safely between electronic

The associate editor coordinating the review of this manuscript and approving it for publication was Flavia Grassi.

devices. Therefore, efficient coding and modulation techniques were developed, and the speed rate was increased to 100 Gbps and 400 Gbps in 2010 and 2014, respectively, where the standard 100GBASE-CR10 of the twin axial copper cable for electrical signaling was released [5].

Since transmission line cables are strictly required in interconnecting high-speed electronic components, high-speed transmission line cables with very low insertion/transfer losses, low crosstalk, low mode conversions, and good signal integrity are required to be designed so that to transfer high-speed data rates. It is worth mentioning that high-speed data rates with 400 Gbps require bandwidths with gigahertz ranges. Hence, the high-speed transmission line cables should be designed to meet the requirement and the standards as defined in 100GBASE-CR1 [6]. However, high-speed cables design is only limited by using commercial software, which mainly depend on full-wave solutions that have unreasonable simulation time. Therefore, the disturbances and nonuniformities of a high-speed cable structure cannot be easily studied using commercial software tools because they do not provide us with the physical model of the investigated phenomena, and their simulation time is very long. Hence, it is impossible to perform thousands of simulations to study the effect of the nonuniformities of the high-speed cables in their normal performance. In [7], balanced and unbalanced high-speed transmission line copper cabler with a longitudinal shield was investigated using the finite element method (FEM), where ''intra-pair skew'' i.e., the propagation time difference between the difference pair lines, was examined using the impulse and step response of the cable. In [8] and [9], the FEM solver in Ansoft HFSS software [10] was used to study the spiral shield of a high-speed cable and its negative effects in generating very narrow stop bands at high frequency region, which is known as the ''suck-out'' effect. In [11], a SPICE circuit model of differential twinax cable from the measured 4-port S-parameters was introduced in order to study the cable transmission properties. In [12], the suck-out effect of high-speed transmission lines was explained by using periodic structure, where the full-wave simulation method was used. Moreover, the electromagnetic compatibility (EMC) of shielded twisted/untwisted pair shielded high-speed transmission line cables for automotive multi-Gig Ethernet application was investigated by using the mixed-mode S parameters in [13].

Additionally, the transmission line theory was widely applied to study different phenomena in transmission line cables [14], [15], [16], [17], [18], [19]. In [14] and [15], an efficient simulation methods of nonlinear transmission lines via model-order reduction and proper orthogonal decomposition were proposed. In [16], signal balancing method was implemented to diminish the mode conversions in imperfectly balanced transmission lines. In [17], transmission line modeling is applied to analysis the dispersion in coaxial lines with higher symmetries. In [18], an extraction method is applied to obtain the characteristic impedance and complex permittivity of transmission lines. Also, in [19], the characteristic impedance of planar transmission lines on lossy substrates was extracted using the method of series resistance.

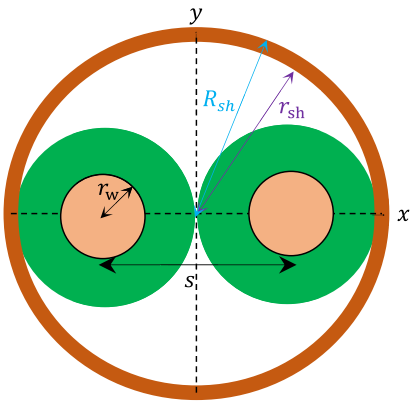

FIGURE 1. Cross-section of a twinax cable.

However, in all the overmentioned papers about high-speed cables, the analysis was restricted only using full-wave solutions provided by commercial software tools or direct measurement testing because there are no accurate theoretical models were developed for the high-speed transmission line cables. Consequently, in this paper, our attention will be focused on developing a transmission line model for the high-speed cables, which is applicable at high-frequency ranges, which help us to understand its physical operation, hence, make the analysis and design of high-speed cables straightforward. To do that, all the side effects of the dielectric and conducting materials should be modeled accurately. It means that the skin and proximity effects of both the inner conductors and the outer shield should be included in the modeling process because their impact on the high-speed cable operation cannot be neglected at the high-frequency range.

This paper is organized as follows. In Section II, the high-speed twinax cable is described, where its per-unit-length (p.u.l) parameters are derived, and also the skin and proximity effect of inner conductors and the shield are formulated analytically. In Section III, a generalized transmission line model is developed for the noncoaxial cable as an intermediate step toward the high-speed cable modeling, where the effect of layered conductors in the AC resistance is discussed. In Section IV, the transmission line model is generalized to the high-speed twinax cables, where the conversions between the common-mode (CM) and differential-mode (DM) signals are studied using the mixed-mode S-parameters. In Section V, the proposed model is validated by comparing its results with one generated by the commercial software tools FEKO and HFSS. In Section VI, experimental testing of actual cables is also conducted to further validate the proposed model. Finally, some conclusions are drawn in Section VII.

II. TWINAX CABLE DESCRIPTION AND MODELLING

The cross-section of a twinax cable is shown in Fig. 1. It consists of two inner conductors with a radius r_w, they are usually

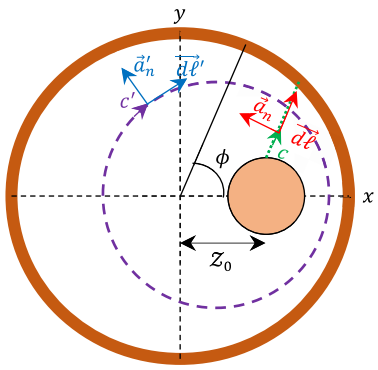

FIGURE 2. The geometry of a noncoaxial cable and the illustration of the integration paths and the normal unit vectors.

called signal lines, separated by a distance s. The two inner conductors are coated by a dielectric, and the whole coated inner conductors are covered by an electric conductor shield with inner and outer radii $r_{\rm sh}$ and $R_{\rm sh}$, respectively. It should be noted that due to the high-frequency range application of the twinax cable that reaches 20 GHz, all skin and proximity effects side effects together with physical phenomena in both conductors and dielectric materials should be carefully considered during the modeling.

A. DERIVATION OF THE PER-UNIT-LENGTH PARAMETERS

Since the twinax cable is attended to operate at a very high frequency, accurate derivation of the p.u.l parameters, which includes the effect of the geometry and curvatures of the cable, is strictly necessary. To obtain the exact expressions of the p.u.l inductance and capacitance of the twinax cable, let us consider a noncoaxial cable in which the inner conductor is shifted from the origin by Z_0 in the x-direction as shown in Fig. 2. The medium between the inner conductor and the shield is considered to be homogenous. Therefore, the transverse electromagnetic (TEM) fields of the noncoaxial cable are given as [20], [21], and [22].

$$\vec{E}_t = 2\pi DV\vec{e}_0 \tag{1a}$$

$$\vec{H}_t = \frac{1}{2\pi D} I\vec{h}_0, \tag{1b}$$

where V and I are the voltage between the inner conductor and the shield, and the current passes through the inner conductor and returns along with the shield, respectively. The constant D is derived for the noncoaxial cable by using a conformal mapping as [20]

$$D = \left(\pi \ln\left(\frac{\alpha\left(\alpha\mathcal{Z}_0 - r_{\rm sh}\right)}{\mathcal{Z}_0 - \alpha r_{\rm sh}}\right)\right)^{-1/2} \tag{2a}$$

$$\alpha = \frac{\left(\mathcal{Z}_0^2 + r_{\rm sh}^2 - r_{\rm w}^2\right) - \sqrt{\left(\mathcal{Z}_0^2 + r_{\rm sh}^2 - r_{\rm w}^2\right)^2 - 4\mathcal{Z}_0^2 r_{\rm sh}^2}}{2\mathcal{Z}_0 r_{\rm sh}}. \tag{2b}$$

The vectors $\vec{e}_0$ and $\vec{h}_0$ are the normalized transverse electric and magnetic fields of the TEM mode, and they are given for the noncoaxial cable in the polar coordinate as [20]

$$\begin{aligned}\vec{e}_0 = -D&\left(\frac{r - \alpha r_{\rm sh}\cos\phi}{r^2 + \alpha^2 r_{\rm sh}^2 - 2\alpha r_{\rm sh} r\cos\phi}\right.\\ &\left. - \frac{\alpha^2 r - \alpha r_{\rm sh}\cos\phi}{\alpha^2 r^2 + r_{\rm sh}^2 - 2\alpha r_{\rm sh} r\cos\phi}\right)\vec{e}_r\\ -D&\left(\frac{1}{r^2 + \alpha^2 r_{\rm sh}^2 - 2\alpha r_{\rm sh} r\cos\phi}\right.\\ &\left. - \frac{1}{\alpha^2 r^2 + r_{\rm sh}^2 - 2\alpha r_{\rm sh} r\cos\phi}\right)\alpha r_{\rm sh}\sin\phi\vec{e}_\phi\end{aligned} \tag{3a}$$

$$\vec{h}_0 = \vec{e}_z \times \vec{e}_0 \tag{3b}$$

It should be noted that (r, ϕ) are the polar coordinates and $\vec{e}_r, \vec{e}_\phi$, and $\vec{e}_z$ are the unit vectors of the cylindrical coordinate.

The self-inductance and capacitance of the inner conductor with respect to the shield are defined as [23]

$$L = -\frac{\int_c \mu\vec{H}_t \cdot \vec{a}_n dl}{\oint_{c'} \vec{H}_t \cdot \vec{dl}'}, \tag{4a}$$

$$C = -\frac{\oint_{c'} \epsilon\vec{E}_{\rm t} \cdot \vec{a}'_n dl'}{\int_c \vec{E}_{\rm t} \cdot \vec{dl}}, \tag{4b}$$

in which $\vec{a}_n$ and $\vec{a}'_n$ are the normal unit vectors to the curves c and c', respectively, as shown in Fig. 2.

It is worth indicating that the paths c and c' can be chosen arbitrarily; however, for simplifying the integration, they are selected to follow the magnetic and electric fields curvatures, respectively. For more details about the magnetic and electric fields distributions in the noncoaxial cable, the reader can refer to [20]

Without losing any generality, the path c' is selected to be the circle, which overlaps the inner surface of the shield, and c is selected as a straight line started at the right edge of the inner conductor and ended at the inner surface of the shield along the x-axis, therefore,

$$\text{path}\,(c') \quad r = r_{\rm sh}, \quad 0 \le \phi \le 2\pi \tag{5a}$$

$$\text{path}\,(c) \quad \phi = 0, \quad \mathcal{Z}_0 + r_{\rm w} \le r \le r_{\rm sh} \tag{5b}$$

Along the path c' the normalized electric and magnetic fields of the TEM mode are given by

$$\vec{e}_0 = -D\frac{1 - \alpha^2}{r_{\rm sh}\left(1 + \alpha^2 - 2\alpha\cos\phi\right)}\vec{e}_r \tag{6a}$$

$$\vec{h}_0 = -D\frac{1 - \alpha^2}{r_{\rm sh}\left(1 + \alpha^2 - 2\alpha\cos\phi_a\right)}\vec{e}_\phi, \tag{6b}$$

whereas along path c, they are given by

$$\vec{e}_0 = -D\left(\frac{1}{r - \alpha r_{\rm sh}} - \frac{\alpha}{\alpha r - b}\right)\vec{e}_r \tag{7a}$$

$$\vec{h}_0 = -D\left(\frac{1}{r - \alpha r_{\rm sh}} - \frac{\alpha}{\alpha r - b}\right)\vec{e}_\phi \tag{7b}$$

By inserting (6a)-(7b) in (4a) and (4b), the self p.u.l inductance and capacitance are obtained as

$$L = \mu \frac{\int_{\mathcal{Z}_0+r_w}^{r_{sh}} \left(\frac{1}{r-\alpha r_{sh}} - \frac{\alpha}{\alpha r-b}\right) dr}{\int_0^{2\pi} \frac{1-\alpha^2}{1+\alpha^2-2\alpha\cos\phi} d\phi} = \mu \frac{\ln\left|\frac{\alpha\mathcal{Z}_0+\alpha r_w-r_{sh}}{r_w-\alpha r_{sh}+\mathcal{Z}_0}\right|}{2\pi} \tag{8a}$$

$$C = \epsilon \frac{2\pi}{\ln\left|\frac{\alpha\mathcal{Z}_0+\alpha r_w-r_{sh}}{r_w-\alpha r_{sh}+\mathcal{Z}_0}\right|} \tag{8b}$$

and

$$\int_0^{2\pi} \frac{1-\alpha^2}{1+\alpha^2-2\alpha\cos\phi} d\phi = 2\pi \tag{8c}$$

is considered in (8a) and (8b). Furthermore, by taking the fact that

$$\left(\frac{\alpha\mathcal{Z}_0+\alpha r_w-r_{sh}}{r_w-\alpha r_{sh}+\mathcal{Z}_0}\right)^2 = \frac{\alpha\left(\alpha\mathcal{Z}_0-r_{sh}\right)}{\mathcal{Z}_0-\alpha r_{sh}}, \tag{9}$$

and the p.u.l. inductance and capacitance can be simplified as

$$L = \frac{\mu}{4\pi^2 D^2} \tag{10a}$$

$$C = \epsilon 4\pi^2 D^2 \tag{10b}$$

It should be indicated that under the condition $r_w \ll r_{sh}$, the obtained L and C will approach the approximate formulas developed by Paul in [23].

B. SKIN AND PROXIMITY EFFECTS OF A TUBULAR SHIELD WITH A NONCOAXIAL INNER CONDUCTOR

According to the Maxwell's equations, the magnetic field inside the tubular conductor can be expressed as

$$\nabla^2\vec{H} - \gamma_{sh}^2\vec{H} = \vec{0}, \tag{11}$$

in which $\gamma_{sh} = \sqrt{j\omega\mu\sigma_{sh}}$ and σ_{sh} is the conductivity of the tubular shield. Due to the symmetry of the tubular conductor shield, the magnetic field has only H_ϕ component in the cylindrical coordinate, hence, (11) can be simplified as

$$r^2\frac{\partial^2 H_\phi}{\partial r^2} + r\frac{\partial H_\phi}{\partial r} - \left(r^2\gamma_{sh}^2+1\right)H_\phi = 0 \tag{12}$$

The solution of equation (12) can be expressed by

$$H_\phi(r) = AI_1(\gamma_{sh}r) + BK_1(\gamma_{sh}r) \tag{13}$$

where I_1 and K_1 are the modified Bessel functions of the first and the second kind of order one, respectively. The constants A and B are determined by using the boundary conditions at the inner and outer surface of the tubular shield and they are expressed as

$$A = \frac{H_{\phi,r_{sh}}K_1(\gamma_{sh}R_{sh}) - H_{\phi,R_{sh}}K_1(\gamma_{sh}r_{sh})}{\Delta} \tag{14a}$$

$$B = \frac{H_{\phi,r_{sh}}I_1(\gamma_{sh}R_{sh}) - H_{\phi,R_{sh}}I_1(\gamma_{sh}r_{sh})}{\Delta} \tag{14b}$$

$$\Delta = I_1(\gamma_{sh}r_{sh})K_1(\gamma_{sh}R_{sh}) - I_1(\gamma_{sh}R_{sh})K_1(\gamma_{sh}r_{sh}) \tag{14c}$$

It should be noted that $H_{\phi,r_{sh}}$ and $H_{\phi,R_{sh}}$ are the magnetic fields at the inner and outer surfaces of the tubular shield, respectively. Therefore, $H_{\phi,r_{sh}}$ can be obtained from (1b) and (3b) by taking $r = r_{sh}$, hence

$$H_{\phi,r_{sh}} = -\frac{I_{in}}{2\pi r_{sh}}\Pi_\phi(\alpha) \tag{15}$$

where

$$\Pi_\phi(\alpha) = \frac{1-\alpha^2}{1+\alpha^2-2\alpha\cos\phi} \tag{16}$$

Noting that I_{in} is the current passing through the inner conductor and return through the inner surface of the tubular shield. Generally, let us consider another current I_{out}, which uniformly flows along the outer surface of the tubular shield and returns through an external return, and it could be a ground plane or another covering shield, therefore

$$H_{\phi,R_{sh}} = \frac{I_{out}}{2\pi R_{sh}} \tag{17}$$

The distribution of the current density within the tubular shield can be obtained from $\vec{\nabla}\times\vec{H} = \vec{J}$ as

$$J_z(r) = \gamma_{sh}\frac{K_1(\gamma_{sh}R_{sh})I_0(\gamma_{sh}r) + I_1(\gamma_{sh}R_{sh})K_0(\gamma_{sh}r)}{\Delta}H_{\phi,r_{sh}} - \gamma_{sh}\frac{I_1(\gamma_{sh}r_{sh})K_0(\gamma_{sh}r) + K_1(\gamma_{sh}r_{sh})I_0(\gamma_{sh}r)}{\Delta}H_{\phi,R_{sh}} \tag{18}$$

whereas the electric field can be obtained from $E_z(r) = J_z(r)/\sigma_{sh}$. Note that I_0 and K_0 are the modified Bessel functions of order zero.

The electric field along the inner and outer surfaces of the tubular shield are given, respectively, as

$$E_z(r_{sh}) = \frac{\gamma_{sh}F_1}{\sigma_{sh}\Delta}H_{\phi,r_{sh}} - \frac{1}{\sigma_{sh}\Delta r_{sh}}H_{\phi,R_{sh}} \tag{19a}$$

$$E_z(R_{sh}) = \frac{1}{\sigma_{sh}\Delta R_{sh}}H_{\phi,r_{sh}} - \frac{\gamma_{sh}F_2}{\sigma_{sh}\Delta}H_{\phi,R_{sh}} \tag{19b}$$

$$F_1 = K_1(\gamma_{sh}R_{sh})I_0(\gamma_{sh}r_{sh}) + I_1(\gamma_{sh}R_{sh})K_0(\gamma_{sh}r_{sh}) \tag{19c}$$

$$F_2 = I_1(\gamma_{sh}r_{sh})K_0(\gamma_{sh}R_{sh}) + K_1(\gamma_{sh}r_{sh})I_0(\gamma_{sh}R_{sh}) \tag{19d}$$

It is indicated that the property $I_1(Z)K_0(Z) + K_1(Z)I_0(Z) = 1/Z$ is used, where Z could be any complex number.

In order to obtain the inner/outer surface impedances p.u.l of the tubular shield, it is better to obtain the p.u.l complex power flowing through the conductor at the inner and outer surface of the shield, hence,

$$P_{in} = -\frac{1}{2}\int_0^{2\pi} E_z(r_{sh}) \times H^*_{\phi,r_{sh}} r_{sh} d\phi \tag{20a}$$

$$P_{out} = \frac{1}{2}\int_0^{2\pi} E_z(R_{sh}) \times H^*_{\phi,R_{sh}} R_{sh} d\phi \tag{20b}$$

Therefore,

$$P_{\text{in}} = \frac{-1}{2}\frac{\gamma_{\text{sh}}F_1}{4\pi^2\sigma_{\text{sh}}\Delta r_{\text{sh}}}|I_{\text{in}}|^2\int_0^{2\pi}\Pi_\phi(\alpha)^2\,d\phi - \frac{1}{2}\frac{1}{4\pi^2\sigma_{\text{sh}}\Delta r_{\text{sh}}R_{\text{sh}}}I_{\text{in}}^*I_{\text{out}}\int_0^{2\pi}\Pi_\phi(\alpha)\,d\phi \quad (21a)$$

$$P_{\text{out}} = \frac{-1}{2}\frac{1}{4\pi^2\sigma_{\text{sh}}\Delta r_{\text{sh}}R_{\text{sh}}}I_{\text{in}}I_{\text{out}}^*\int_0^{2\pi}\Pi_\phi(\alpha)\,d\phi - \frac{1}{2}\frac{\gamma_{\text{sh}}F_2}{2\pi\sigma_{\text{sh}}\Delta R_{\text{sh}}}|I_{\text{out}}|^2 \quad (21b)$$

and,

$$\int_0^{2\pi}\Pi_\phi(\alpha)\,d\phi = 2\pi \quad \text{and}$$
$$\int_0^{2\pi}\Pi_\phi(\alpha)^2\,d\phi = 2\pi\frac{1+\alpha^2}{1-\alpha^2} \quad (21c)$$

By considering the definition of the p.u.l complex power $P = \frac{1}{2}Z|I|^2$, hence, (21a) and (21b) can be written as

$$P_{\text{in}} = \frac{1}{2}Z_{\text{sh}}^{\text{in}}|I_{\text{in}}|^2 + \frac{1}{2}Z_{\text{t}}I_{\text{in}}^*I_{\text{out}} \quad (22a)$$

$$P_{\text{out}} = \frac{1}{2}Z_{\text{t}}I_{\text{in}}I_{\text{out}}^* + \frac{1}{2}Z_{\text{sh}}^{\text{out}}|I_{\text{out}}|^2 \quad (22b)$$

In which Z_{in} and Z_{out} are the inner and outer p.u.l surface impedances of the tubular shield, respectively, and Z_{t} is the p.u.l transfer impedance of the shield. They can be expressed as

$$Z_{\text{sh}}^{\text{in}} = \frac{-\gamma_{\text{sh}}F_1}{2\pi\sigma_{\text{sh}}\Delta r_{\text{sh}}}\frac{1+\alpha^2}{1-\alpha^2} \quad (23a)$$

$$Z_{sh}^{\text{out}} = \frac{-\gamma_{\text{sh}}F_2}{2\pi\sigma_{\text{sh}}\Delta R_{\text{sh}}} \quad (23b)$$

$$Z_{\text{t}} = \frac{-1}{2\pi\sigma_{\text{sh}}\Delta r_{\text{sh}}R_{\text{sh}}} \quad (23c)$$

As compared to the results obtained by Schelkunoff in [24] for the coaxial cable, the outer surface and transfer impedances have the same form. However, the inner transfer impedance is different by the factor $\frac{1+\alpha^2}{1-\alpha^2}$ due to the fact that the current in the inner surface of the shield tends to accumulate near the inner conductor side, which is not located in the middle of the shield, as shown in Fig. 2. It means that the inner impedance is increased by the factor $\frac{1+\alpha^2}{1-\alpha^2} > 1$, due to the fact that the inner current is not uniformly distributed along the shield because the inner conductor is not centrally located. Also, another interesting result is obtained, which is the transfer impedance remained unchanged, when the current outside the shield is assumed to be uniform even if the inner current is not uniformly distributed in the inner surface shield. However, if the outer current is also nonuniform along the shield, the transfer impedance will depend on both nonuniformities factors of the inner and outer currents.

C. SKIN AND PROXIMITY EFFECTS OF A LAYERED INNER CONDUCTOR IN A NONCOAXIAL CABLE

Double layered inner conductor with the conductor conductivities σ_1 and σ_2, respectively. Their corresponding radii are

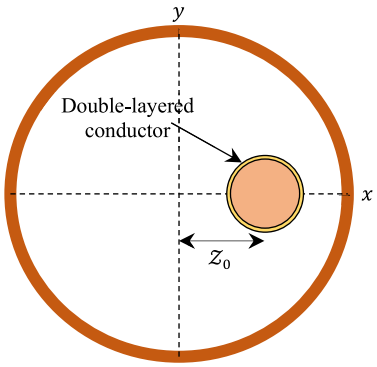

FIGURE 3. The geometry of a noncoaxial cable with double layered inner conductor.

r_{w_1} and r_{w_2} as shown in Fig. 3. By applying the same analysis done above on the current density $\vec{J}$ in the cross-section of the double-layered conductor, the following results are obtained as [25]:

$$J_z(r) = \begin{cases} c_1 I_0(\gamma_1 r), & 0 \le r \le r_{\text{w}_1} \\ d_1 I_0(\gamma_2 r) + d_2 K_0(\gamma_2 r), & r_{\text{w}_1} < r \le r_{\text{w}_2} \end{cases} \quad (24)$$

where $\gamma_i = \sqrt{j\omega\mu\sigma_i}$

Therefore, the electric and magnetic fields within the double-layered conductor, respectively, are described as

$$E_z(r) = \begin{cases} \frac{c_1}{\sigma_1}I_0(\gamma_1 r), & 0 \le r \le r_{\text{w}_1} \\ \frac{d_1}{\sigma_2}I_0(\gamma_2 r) + \frac{d_2}{\sigma_2}K_0(\gamma_2 r), & r_{\text{w}_1} \le r \le r_{\text{w}_2} \end{cases} \quad (25a)$$

$$H_\phi(r) = \begin{cases} \frac{c_1}{\gamma_1}I_1(\gamma_1 r), & 0 \le r \le r_{\text{w}_1} \\ \frac{d_1}{\gamma_2}I_1(\gamma_2 r) - \frac{d_2}{\gamma_2}K_1(\gamma_2 r), & r_{\text{w}_1} \le r \le r_{\text{w}_2} \end{cases} \quad (25b)$$

By applying the electric and magnetic fields boundary conditions at the layer's boundaries [26], i.e., $E_z|_{r=r_{\text{w}_1}-} = E_z|_{r=r_{\text{w}_1}+}$ and $H_\phi|_{r=r_{\text{w}_1}-} = H_\phi|_{r=r_{\text{w}_1}+}$, respectively, where the magnetic permeability is considered the same in both conductors. hence, the constants d_1 and d_2 are obtained in terms of c_1 as

$$d_1 = c_1\gamma_2 r_{\text{w}_1}\left(\frac{\sigma_2}{\sigma_1}I_0(\gamma_1 r_{\text{w}_1})K_1(\gamma_2 r_{\text{w}_1}) + \frac{\gamma_2}{\gamma_1}I_1(\gamma_1 r_{\text{w}_1})K_0(\gamma_2 r_{\text{w}_1})\right) \quad (26a)$$

$$d_2 = c_1\gamma_2 r_{\text{w}_1}\left(\frac{\sigma_2}{\sigma_1}I_1(\gamma_2 r_{\text{w}_1})I_0(\gamma_1 r_{\text{w}_1}) - \frac{\gamma_2}{\gamma_1}I_0(\gamma_2 r_{\text{w}_1})I_1(\gamma_1 r_{\text{w}_1})\right) \quad (26b)$$

To determine the constant c_1, the magnetic along the outer layer of the inner conductor should be used. From (3a), the magnetic field along the layered

conductor can be obtained as

$$H_\phi\left(r_{w_2}\right) = -\frac{I_{in}}{2\pi r_{w_2}} \frac{r_{sh}\mathcal{Z}_0\left(1-\alpha^2\right)}{\alpha\left(r_{sh}^2 - r_{w_2}^2 - \mathcal{Z}_0^2 - 2r_{w_2}\mathcal{Z}_0\cos\phi\right)} \tag{27}$$

Since $d_1 = c_1\mathfrak{m}_1$ and $d_2 = c_2\mathfrak{m}_2$, therefore

$$c_1 = \frac{-\gamma_2 I_{in}}{2\pi r_{w_2}\left(\mathfrak{m}_1 I_0\left(\gamma_2 r_{w_2}\right) - \mathfrak{m}_2 K_0\left(\gamma_2 r_{w_2}\right)\right)} \times \frac{r_{sh}\mathcal{Z}_0\left(1-\alpha^2\right)}{\alpha\left(r_{sh}^2 - r_{w_2}^2 - \mathcal{Z}_0^2 - 2r_{w_2}\mathcal{Z}_0\cos\phi\right)} \tag{28}$$

Once again, by applying the definition of the p.u.l complex power, the p.u.l inner impedance of the layered conductor is obtained as

$$Z_{cond} = \frac{\gamma_2}{2\pi\sigma_2 r_{w_2}} \frac{\mathfrak{m}_1 I_0\left(\gamma_2 r_{w_2}\right) + \mathfrak{m}_2 K_0\left(\gamma_2 r_{w_2}\right)}{\mathfrak{m}_1 I_1\left(\gamma_2 r_{w_2}\right) - \mathfrak{m}_2 K_1\left(\gamma_2 r_{w_2}\right)} \frac{r_{sh}^2 - r_{w_2}^2 - \mathcal{Z}_0^2}{r_{sh}\mathcal{Z}_0(1-\alpha^2)}\alpha \tag{29a}$$

and

$$\lim_{\mathcal{Z}_0 \to 0}\left(\frac{r_{sh}^2 - r_{w_2}^2 - \mathcal{Z}_0^2}{r_{sh}\mathcal{Z}_0(1-\alpha^2)}\alpha\right) = 1 \tag{29b}$$

means that the inner conductor is centered at the origin of the tubular shield, hence, Z_{cond} is reduced to the expression of an isolated/coaxial wire [25]. This indicated that the factor $\frac{r_{sh}^2 - r_{w_2}^2 - \mathcal{Z}_0^2}{r_{sh}\mathcal{Z}_0(1-\alpha^2)}\alpha$ represents the proximity effect of the outer shield, due to the noncoaxial location of the inner conductor. For the case of a non-layered conductor, i.e., $\sigma_1 = \sigma_2 = \sigma$, and by taking $r_{w_2} = r_w$, Z_{cond} is simplified as

$$Z_{cond} = \frac{\gamma}{2\pi\sigma r_w} \frac{I_0\left(\gamma r_w\right)}{I_1\left(\gamma r_w\right)} \frac{r_{sh}^2 - r_w^2 - \mathcal{Z}_0^2}{r_{sh}\mathcal{Z}_0(1-\alpha^2)}\alpha \tag{30}$$

III. TRANSMISSION LINE MODEL OF A NONCOAXIAL CABLE

In this section, the transmission line model is applied to the noncoaxial cable, where all the side effects such as skin and proximity effects are included. Moreover, it should be indicated that the transmission line model is only valid under the condition $\lambda \gg r_{sh}$, and λ is the operating wavelength.

A. TRANSMISSION LINE EQUATIONS

The transmission line equations of the noncoaxial cable can be formulated as [23]

$$\frac{dV(z,f)}{dz} + Z_{cable}(f)\, I(z,f) = 0 \tag{31a}$$

$$\frac{dI(z,f)}{dz} + Y_{cable}(f)\, V(z,f) = 0 \tag{31b}$$

where $V(z,f)$ and $I(z,f)$ are the voltage and currents of the noncoaxial cable at a given operating frequency f, Z_{cable} and Y_{cable} are the p.u.l impedance and admittance, and they are expressed as

$$Z_{cable}(f) = Z_{cond}(f) + Z_{sh}^{in}(f) + j2\pi f L \tag{32a}$$

$$Y_{cable}(f) = 2\pi f\left(\tan\delta_{Loss} + j\right) C \tag{32b}$$

The term $\tan\delta_{Loss}$ represents the loss tangent, due to the bound charge and dipole relaxation in the dielectric material [26].

B. TRANSMISSION LINE SOLUTION AND S-PARAMETERS REPRESENTATION

The solution of the transmission line equations (31a) and (31b) can be obtained in terms of the transfer parameters as

$$\mathbf{\Phi}(\mathcal{L}) = \begin{bmatrix} \cosh\gamma_T\mathcal{L} & Z_c\sinh\gamma_T\mathcal{L} \\ Z_c^{-1}\sinh\gamma_T\mathcal{L} & \cosh\gamma_T\mathcal{L} \end{bmatrix} \tag{33}$$

where $\mathcal{L}$ is the length of the noncoaxial cable, Z_c its characteristic impedance, γ_T is the propagation constant, and

$$Z_c = \sqrt{\frac{Z_{cable}(f)}{Y_{cable}(f)}} \tag{34a}$$

$$\gamma_T = \sqrt{Z_{cable}(f)\, Y_{cable}(f)} \tag{34b}$$

Consequently, the S-parameters of the noncoaxial cable are given as [27]

$$\boldsymbol{S} = \begin{bmatrix} s_{11} & s_{12} \\ s_{21} & s_{22} \end{bmatrix} \tag{35}$$

where

$$s_{11} = s_{22} = \frac{\left(Z_c^2 - Z_0^2\right)\sinh\gamma_T\mathcal{L}}{2Z_0 Z_c\cosh\gamma_T\mathcal{L} + \left(Z_c^2 + Z_0^2\right)\sinh\gamma_T\mathcal{L}} \tag{36a}$$

$$s_{21} = s_{12} = \frac{2Z_0 Z_c}{2Z_0 Z_c\cosh\gamma_T\mathcal{L} + \left(Z_c^2 + Z_0^2\right)\sinh\gamma_T\mathcal{L}} \tag{36b}$$

where Z_0 is the S-parameter's reference impedance.

C. NUMERICAL RESULTS AND VALIDATION

In order to validate the expressions of the skin and proximity effects, a noncoaxial cable is considered, where the inner wire is a double-layered conductor. The parameters of the noncoaxial cable are taken as: the inner wire is copper with a radius $r_{w_1} = 0.2675$ mm, and covered with tin layer has thickness $t_{tin} = 5\ \mu$m, the outer shield is aluminum with a radius $r_{sh} = 1.56$ mm and thickness $t_{AL} = 0.13$ mm. At first, the dielectric material is considered to be air, i.e., lossless and homogeneous, so as to make the validation straightforward. It is seen that the transmission line model is valid under the condition $\lambda > 2(r_{sh} - r_w)$, which ensures only the propagation of the TEM mode [22]. It is indicated that the modified Bessel functions do not give correct results for large function arguments. To overcome this problem, the method proposed in [28] is used in this paper. The results of the skin and proximity effect for different inner cable positions are shown in Fig. 4. It can be observed that the current density tends to accumulate at the edge side located at the closest return path in both the inner conductor and the shield.

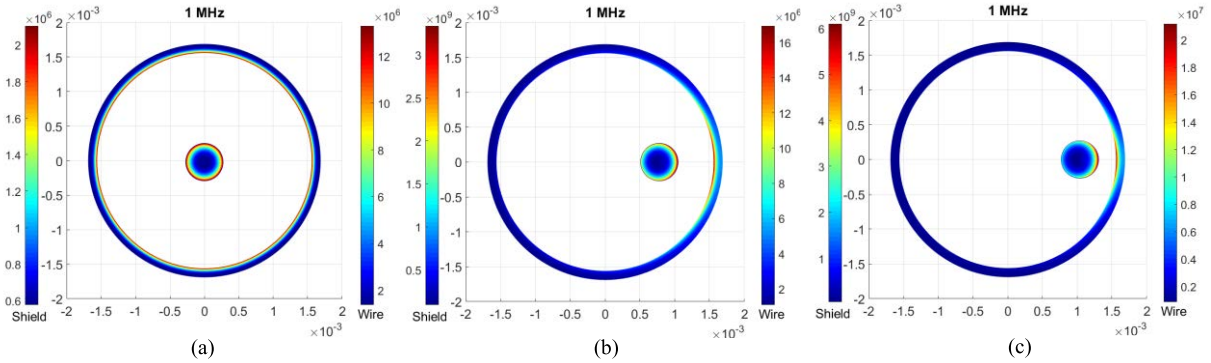

FIGURE 4. Current density distribution within the inner conductor and the outer shield. (a) $\mathcal{Z}_0 = 0$. (b) $\mathcal{Z}_0 = r_{sh}/2$. (c) $\mathcal{Z}_0 = 2r_{sh}/3$.

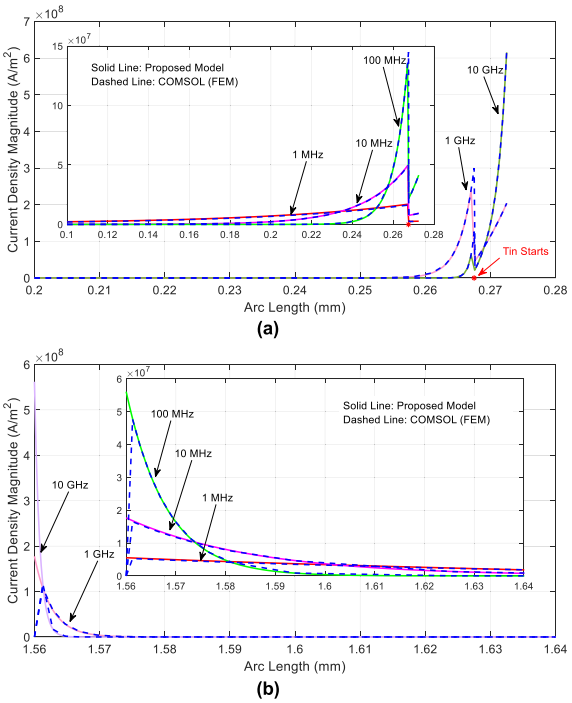

FIGURE 5. Current density magnitude distribution of a noncoaxial cable with $\mathcal{Z}_0 = r_{sh}/2$. (a) Inner conductor. (b) Outer shield.

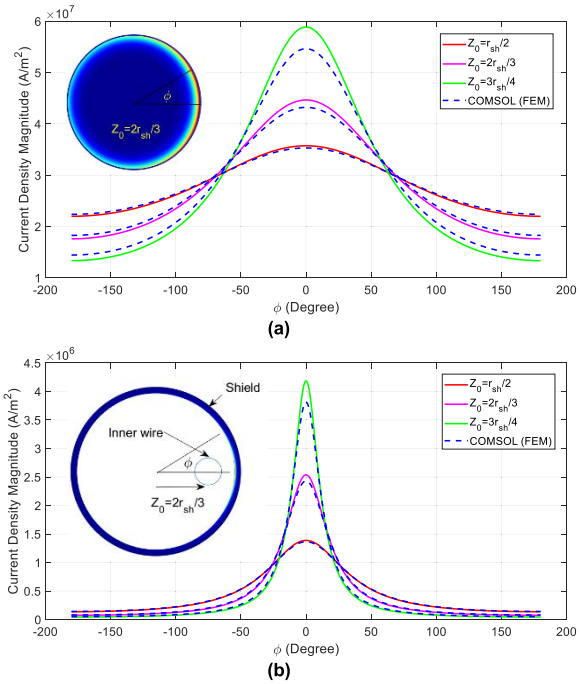

FIGURE 6. Current density magnitude at 10 MHz along a circular path with radius 0.26 mm and 1.625 mm within the inner conductor and shield, respectively. (a) Inner conductor. (b) Outer shield.

Moreover, Figs. 5 (a) and (b) show the current density magnitude distribution along the straight paths ($\phi = 0$) within the inner conductor and the shield surfaces. It can be observed that a good agreement is obtained between the results of our proposed model and the one generated by COMSOL software [29]. It is also seen that the current density has very low intensity in the Tin layer at lower frequencies, but it has higher intensity at high frequency region as indicated in the 10 GHz case, in which the current distribution has the highest concentration at the Tin layer.

In addition, Figs. 6 (a) and (b) show the current density magnitude distributions along the circular paths within the inner conductor and shield surfaces, and also a good agreement is obtained between the proposed model and COMSOL software. Here, the current densities are accumulated at the closest edge between the inner conductor and the shield for such a noncoaxial cable. Note that Figs. 6 (a) and (b) validate the ϕ-depend factors shown in (27) and (16), respectively.

Therefore, the AC resistance of the inner wire and the shield increase due to the skin and proximity effects as presented in Eqs. (23a), (29), and (30), and the results are shown in Fig. 7. Also, it can be observed that the position of the inner conductor has a considerable effect on the AC inductance of both inner conductor and shield. Moreover, it can be deduced that the Tinned layered conductor has higher AC resistance and inductance at high frequency region as compared to the untinned conductor because the Tin has lower conductivity than the copper, and most of the current flow in Tin layers at high frequency. Whereas, at low frequency region the AC resistance of the Tinned and untinned conductors are identical

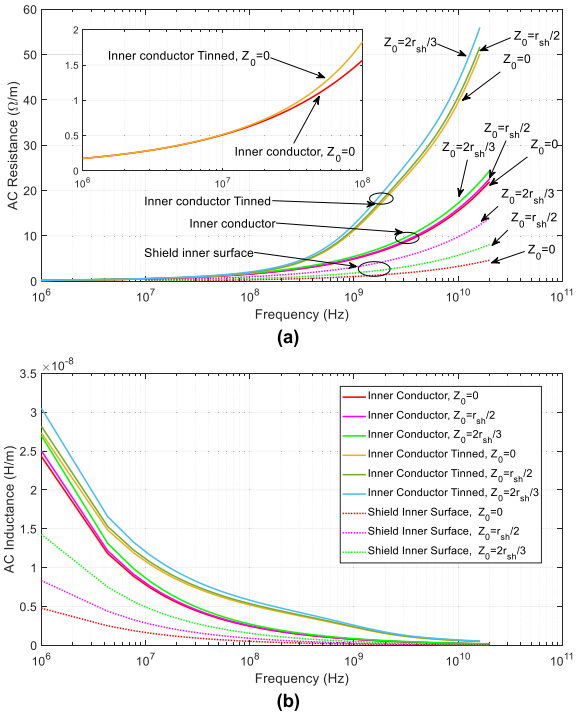

FIGURE 7. The AC resistance and inductance of noncoaxial cable with and without Tin layer. (a) AC resistance. (b) AC inductance.

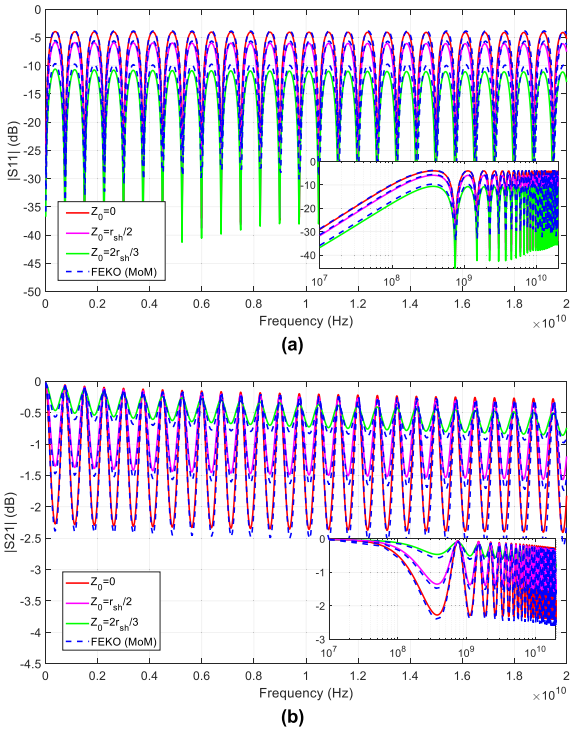

FIGURE 8. The S-parameters of a noncoaxial with different inner conductor positions. (a) S_{11} parameter is the return loss. (b) S_{21} parameter is the insertion loss.

because the currents density is mainly flows in copper core as shown in Figs. 5 (a) and 7 (a).

To perform a further validation, a noncoaxial cable with total length $\mathcal{L} = 0.2$ m is considered, where the inner conductor is taken to be copper, and the thickness of the aluminum shield is assumed to be $t_{\mathrm{AL}} = 9\ \mu$m. The results of the S-parameters of the noncoaxial cable with different inner conductor positions are shown in Fig. 8. The validation is performed by comparing the results with one generated by the commercial software FEKO [30], and perfect agreements are obtained.

IV. TRANSMISSION LINE MODEL OF A TWINAX CABLE

The transmission line theory is generalized to be applicable to high-speed twinax cables with an arbitrary cross-section. The primary purpose is to investigate the effect of the cable geometry on its performance and also investigate the longitudinal conversion loss (LCL) and transverse conversion loss (TCL) of the cable.

A. TRANSMISSION LINE EQUATIONS OF TWINAX CABLE

The transmission line equations of the twinax cable can be formulated as [23]

$$\frac{d\boldsymbol{V}(z,f)}{dz} + \boldsymbol{Z}(f)\boldsymbol{I}(z,f) = \boldsymbol{0}, \tag{37a}$$

$$\frac{d\boldsymbol{I}(z,f)}{dz} + \boldsymbol{Y}(f)\boldsymbol{V}(z,f) = \boldsymbol{0}. \tag{37b}$$

where $\boldsymbol{Z}(f)$, $\boldsymbol{Y}(f)$ are the p.u.l impedance and admittance matrices of the twinax cable and they are given as

$$\boldsymbol{Z}(f) = \begin{bmatrix} Z_{11} & Z_{12} \\ Z_{12} & Z_{22} \end{bmatrix} = \boldsymbol{Z}_{\mathrm{ac\_Imp}} + j2\pi f\boldsymbol{L} \tag{38a}$$

$$\boldsymbol{Y}(f) = \begin{bmatrix} Y_{11} & Y_{12} \\ Y_{12} & Y_{22} \end{bmatrix} = 2\pi f\,(\tan\delta_{\mathrm{Loss}} + j)\,\boldsymbol{C} \tag{38b}$$

In which $\boldsymbol{L}$ and $\boldsymbol{C}$ are the p.u.l inductance and capacitance of the twinax cable, and $\boldsymbol{Z}_{\mathrm{ac\_Imp}}$ is the p.u.l ac impedance of the conductors and the shield and it can be formulated as

$$\boldsymbol{Z}_{\mathrm{ac\_Imp}} = \begin{bmatrix} Z_{\mathrm{con1}} + Z^{\mathrm{in}}_{\mathrm{sh1}} & Z^{\mathrm{in}}_{\mathrm{sh12}} \\ Z^{\mathrm{in}}_{\mathrm{sh12}} & Z_{\mathrm{con2}} + Z^{\mathrm{in}}_{\mathrm{sh2}} \end{bmatrix} \tag{39}$$

When conductors 1 and 2 of twinax cable are located in the x-axis at $\mathcal{Z}_1$ and $\mathcal{Z}_2$, respectively, then

$$Z_{\mathrm{con1/2}} = \frac{\gamma}{2\pi\sigma r_{\mathrm{w}}}\frac{I_0(\gamma r_{\mathrm{w}})}{I_1(\gamma r_{\mathrm{w}})}\frac{r_{\mathrm{sh}}^2 - r_{\mathrm{w}}^2 - \mathcal{Z}_{1/2}^2}{r_{\mathrm{sh}}\mathcal{Z}_{1/2}(1-\alpha_{1/2}^2)}\alpha_{1/2} \tag{40a}$$

$$Z^{\mathrm{in}}_{\mathrm{sh1/2}} = \frac{-\gamma_{\mathrm{sh}}F_1}{2\pi\sigma_{\mathrm{sh}}\Delta r_{\mathrm{sh}}}\frac{1+\alpha_{1/2}^2}{1-\alpha_{1/2}^2} \tag{40b}$$

$$Z^{\mathrm{in}}_{\mathrm{sh12}} = \frac{-\gamma_{\mathrm{sh}}F_1}{2\pi\sigma_{\mathrm{sh}}\Delta r_{\mathrm{sh}}}\frac{\alpha_1(1-\alpha_2^2) - \alpha_2(1-\alpha_1^2)}{\alpha_1(1+\alpha_2^2) - \alpha_2(1+\alpha_1^2)} \tag{40c}$$

It is worth noticing that for layered conductors, the expression (29) should be used instead of (30) in (40a).

B. MODAL DOMAIN FORMULATION

In this section, the modal domain decomposition is performed in order to investigate the CM and DM modes and

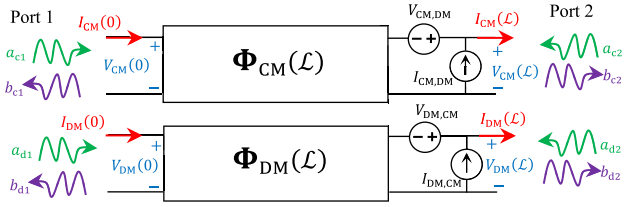

FIGURE 9. The modal domain solution of the high-speed transmission line equations.

the conversions between them by using the mixed-mode S-parameters. The conversions between the modes are the LCL, i.e., CM-to-DM and TCL, i.e., DM-to-CM. The modal voltages and currents are defined as [31]

$$\underbrace{\begin{bmatrix} V_1 \\ V_2 \end{bmatrix}}_{\boldsymbol{V}} = \underbrace{\begin{bmatrix} 1 & 1/2 \\ 1 & -1/2 \end{bmatrix}}_{\boldsymbol{T_V}} \underbrace{\begin{bmatrix} V_{\mathrm{CM}} \\ V_{\mathrm{DM}} \end{bmatrix}}_{\boldsymbol{V_{\mathrm{M}}}},$$
$$\underbrace{\begin{bmatrix} I_1 \\ I_2 \end{bmatrix}}_{\boldsymbol{I}} = \underbrace{\begin{bmatrix} 1/2 & 1 \\ 1/2 & -1 \end{bmatrix}}_{\boldsymbol{T_I}} \underbrace{\begin{bmatrix} I_{\mathrm{CM}} \\ I_{\mathrm{DM}} \end{bmatrix}}_{\boldsymbol{I_{\mathrm{M}}}}. \tag{41}$$

The transmission line equations of the twinax cable (37a) and (37b) can be written in the modal domain as

$$\frac{d\boldsymbol{V}_{\mathrm{M}}(z,f)}{dz} + \boldsymbol{Z}_{\mathrm{M}}(f)\,\boldsymbol{I}_{\mathrm{M}}(z,f) = \boldsymbol{0}, \tag{42a}$$
$$\frac{d\boldsymbol{I}_{\mathrm{M}}(z,f)}{dz} + \boldsymbol{Y}_{\mathrm{M}}(f)\,\boldsymbol{V}_{\mathrm{M}}(z,f) = \boldsymbol{0}. \tag{42b}$$

where

$$\boldsymbol{Z}_{\mathrm{M}}(f) = \boldsymbol{T}_V^{-1}\boldsymbol{Z}(f)\,\boldsymbol{T}_I = \begin{bmatrix} Z_{\mathrm{CM}} & \Delta Z \\ \Delta Z & Z_{\mathrm{DM}} \end{bmatrix} \tag{43a}$$
$$\boldsymbol{Y}_{\mathrm{M}}(f) = \boldsymbol{T}_I^{-1}\boldsymbol{Y}(f)\,\boldsymbol{T}_V = \begin{bmatrix} Y_{\mathrm{CM}} & \Delta Y \\ \Delta Y & Y_{\mathrm{DM}} \end{bmatrix} \tag{43b}$$

in which

$$Z_{\mathrm{CM}} = (Z_{11} + Z_{22} + 2Z_{12})/4 \tag{44a}$$
$$Z_{\mathrm{DM}} = Z_{11} + Z_{22} - 2Z_{12} \tag{44b}$$
$$\Delta Z = (Z_{11} - Z_{22})/2 \tag{44c}$$
$$Y_{\mathrm{CM}} = Y_{11} + Y_{22} + 2Y_{12} \tag{44d}$$
$$Y_{\mathrm{DM}} = (Y_{11} + Y_{22} - 2Y_{12})/4 \tag{44e}$$
$$\Delta Y = (Y_{11} - Y_{22})/2 \tag{44f}$$

Therefore, (42a) and (42b) can be written as

$$\frac{dV_{\mathrm{CM}}(z,f)}{dz} + Z_{\mathrm{CM}} I_{\mathrm{CM}}(z,f) = -\Delta Z I_{\mathrm{DM}}(z,f), \tag{45a}$$
$$\frac{dI_{\mathrm{CM}}(z,f)}{dz} + Y_{\mathrm{CM}} V_{\mathrm{CM}}(z,f) = -\Delta Y V_{\mathrm{DM}}(z,f), \tag{45b}$$
$$\frac{dV_{\mathrm{DM}}(z,f)}{dz} + Z_{\mathrm{DM}} I_{\mathrm{DM}}(z,f) = -\Delta Z I_{\mathrm{CM}}(z,f), \tag{45c}$$
$$\frac{dI_{\mathrm{DM}}(z,f)}{dz} + Y_{\mathrm{DM}} V_{\mathrm{DM}}(z,f) = -\Delta Y V_{\mathrm{CM}}(z,f). \tag{45d}$$

It can be observed that transmission line equations of the CM and DM signals are coupled with each other due to the factors ΔZ and ΔY, which they represent the geometric imbalance of the high-speed transmission line cable [31], [32], and they are responsible for the conversions between the modes, i.e., LCL and TCL. Therefore, the modal domain solution of the transmission line equations is shown in Fig. 9, where a_{ci}/ b_{ci} and $a_{\mathrm{d}i}$/ $b_{\mathrm{d}i}$ are the modal incident/ reflected waves at port i for the CM and DM signals, respectively, and they are defined as [33] and [34]

$$a_{\mathrm{c1}} = \frac{V_{\mathrm{CM}}(0) + Z_{\mathrm{CM_0}} I_{\mathrm{CM}}(0)}{2\sqrt{Z_{\mathrm{CM_0}}}},$$
$$a_{\mathrm{c2}} = \frac{V_{\mathrm{CM}}(\mathcal{L}) - Z_{\mathrm{CM_0}} I_{\mathrm{CM}}(\mathcal{L})}{2\sqrt{Z_{\mathrm{CM_0}}}} \tag{46a}$$
$$b_{\mathrm{c1}} = \frac{V_{\mathrm{CM}}(0) - Z_{\mathrm{CM_0}} I_{\mathrm{CM}}(0)}{2\sqrt{Z_{\mathrm{CM_0}}}},$$
$$b_{\mathrm{c2}} = \frac{V_{\mathrm{CM}}(\mathcal{L}) + Z_{\mathrm{CM_0}} I_{\mathrm{CM}}(\mathcal{L})}{2\sqrt{Z_{\mathrm{CM_0}}}} \tag{46b}$$
$$a_{d1} = \frac{V_{\mathrm{DM}}(0) + Z_{\mathrm{DM_0}} I_{\mathrm{DM}}(0)}{2\sqrt{Z_{\mathrm{DM_0}}}},$$
$$a_{d2} = \frac{V_{DM}(\mathcal{L}) - Z_{\mathrm{DM_0}} I_{\mathrm{DM}}(\mathcal{L})}{2\sqrt{Z_{\mathrm{DM_0}}}} \tag{46c}$$
$$b_{d1} = \frac{V_{\mathrm{DM}}(0) - Z_{\mathrm{DM_0}} I_{\mathrm{DM}}(0)}{2\sqrt{Z_{\mathrm{DM_0}}}},$$
$$b_{d2} = \frac{V_{\mathrm{DM}}(\mathcal{L}) + Z_{\mathrm{DM_0}} I_{\mathrm{DM}}(\mathcal{L})}{2\sqrt{Z_{\mathrm{DM_0}}}} \tag{46d}$$

where

$$\boldsymbol{\Phi}_{\mathrm{CM}}(\mathcal{L}) = \begin{bmatrix} \cosh\gamma_{\mathrm{CM}}\mathcal{L} & -Z_{\mathrm{CM}_c}\sinh\gamma_{\mathrm{CM}}\mathcal{L} \\ -Z_{\mathrm{CM}_c}^{-1}\sinh\gamma_{\mathrm{CM}}\mathcal{L} & \cosh\gamma_{\mathrm{CM}}\mathcal{L} \end{bmatrix} \tag{47a}$$
$$\boldsymbol{\Phi}_{\mathrm{DM}}(\mathcal{L}) = \begin{bmatrix} \cosh\gamma_{\mathrm{DM}}\mathcal{L} & -Z_{\mathrm{DM}_c}\sinh\gamma_{\mathrm{DM}}\mathcal{L} \\ -Z_{\mathrm{DM}_c}^{-1}\sinh\gamma_{\mathrm{DM}}\mathcal{L} & \cosh\gamma_{\mathrm{DM}}\mathcal{L} \end{bmatrix} \tag{47b}$$

and

$$Z_{\mathrm{CM}_c} = \sqrt{\frac{Z_{\mathrm{CM}}}{Y_{\mathrm{CM}}}}, \quad Z_{\mathrm{DM}_c} = \sqrt{\frac{Z_{\mathrm{DM}}}{Y_{\mathrm{DM}}}} \tag{48a}$$
$$\gamma_{\mathrm{CM}} = \sqrt{Z_{\mathrm{CM}} Y_{\mathrm{CM}}}, \quad \gamma_{\mathrm{DM}} = \sqrt{Z_{\mathrm{DM}} Y_{\mathrm{DM}}} \tag{48b}$$
$$Z_{\mathrm{CM_0}} = Z_0/2, \quad Z_{\mathrm{DM_0}} = 2Z_0 \tag{48c}$$

It is indicated that $V_{\mathrm{CM,DM}}$ or $V_{\mathrm{DM,CM}}$ and $I_{\mathrm{CM,DM}}$ or $I_{\mathrm{DM,CM}}$ are the total voltage and current due to DM-to-CM or CM-to-DM conversion:

$$\begin{bmatrix} V_{\mathrm{CM,DM}} \\ I_{\mathrm{CM,DM}} \end{bmatrix} = \int_0^{\mathcal{L}} \boldsymbol{\Phi}_{\mathrm{CM}}(\mathcal{L} - z) \begin{bmatrix} -\Delta Z I_{\mathrm{DM}}(z,f) \\ -\Delta Y V_{\mathrm{DM}}(z,f) \end{bmatrix} dz \tag{49a}$$

$$\begin{bmatrix} V_{\mathrm{DM,CM}} \\ I_{\mathrm{DM,CM}} \end{bmatrix} = \int_0^{\mathcal{L}} \boldsymbol{\Phi}_{\mathrm{DM}}(\mathcal{L} - z) \begin{bmatrix} -\Delta Z I_{\mathrm{CM}}(z,f) \\ -\Delta Y V_{\mathrm{CM}}(z,f) \end{bmatrix} dz \tag{49b}$$

It can be observed from Eqs. (45) and (49) that the CM and DM signals are coupled with each other. Hence, the solution of the equation cannot be obtained directly. To simplify the

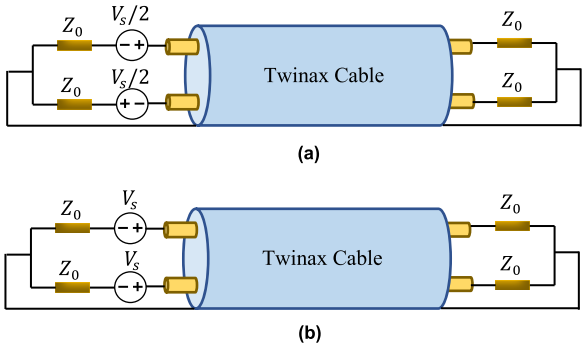

FIGURE 10. Balanced input/output terminals of the twinax cable. (a) DM excitation. (b) CM excitation.

analysis, the concept of weak balance is used [31], [32]. It means that the input and output terminals should be considered well-balanced, where DM and CM excitations are considered separately to investigate LCL and TCL conversions, respectively.

For the DM excitation, the input/output terminals are taken as shown in Fig.10 (a). Therefore,

$$V_{\mathrm{DM}}(0) = V_s - Z_{\mathrm{DM}_0} I_{\mathrm{DM}}(0) \tag{50a}$$
$$V_{\mathrm{DM}}(\mathcal{L}) = Z_{\mathrm{DM}_0} I_{\mathrm{DM}}(\mathcal{L}) \tag{50b}$$
$$V_{\mathrm{CM}}(0) = -Z_{\mathrm{CM}_0} I_{\mathrm{CM}}(0) \tag{50c}$$
$$V_{\mathrm{CM}}(\mathcal{L}) = Z_{\mathrm{CM}_0} I_{\mathrm{CM}}(\mathcal{L}) \tag{50d}$$

Since the input/output terminals of the highspeed twinax cable are assumed to be well-balanced, then the CM-to-DM conversion sources $V_{\mathrm{DM,CM}}$ and $I_{\mathrm{DM,CM}}$ can be neglected due their minor effect [31], [32]. Therefore, the DM voltage and currents along the highspeed twinax cable are determined as

$$\begin{bmatrix} V_{\mathrm{DM}}(z,f) \\ I_{\mathrm{DM}}(z,f) \end{bmatrix} = \mathbf{\Phi}_{\mathrm{DM}}(z-\mathcal{L}) \begin{bmatrix} V_{\mathrm{DM}}(\mathcal{L}) \\ I_{\mathrm{DM}}(\mathcal{L}) \end{bmatrix} \tag{51}$$

in which

$$V_{\mathrm{DM}}(\mathcal{L}) = \frac{Z_{\mathrm{DM}_c} Z_{\mathrm{DM}_0}}{\Delta_{\mathrm{DM}}} V_s \tag{52a}$$
$$I_{\mathrm{DM}}(\mathcal{L}) = \frac{Z_{\mathrm{DM}_c}}{\Delta_{\mathrm{DM}}} V_s \tag{52b}$$
$$\Delta_{\mathrm{DM}} = 2 Z_{\mathrm{DM}_0} Z_{\mathrm{DM}_c} \cosh \gamma_{\mathrm{DM}} \mathcal{L} + \left(Z_{\mathrm{DM}_c}^2 + Z_{\mathrm{DM}_0}^2 \right) \sinh \gamma_{\mathrm{DM}} \mathcal{L} \tag{52c}$$

By using (51), (49a) can be reformulated as

$$\begin{bmatrix} V_{\mathrm{CM,DM}} \\ I_{\mathrm{CM,DM}} \end{bmatrix} = \begin{bmatrix} \Psi_{11}^{\mathrm{CM,DM}}(\mathcal{L}) & \Psi_{12}^{\mathrm{CM,DM}}(\mathcal{L}) \\ \Psi_{21}^{\mathrm{CM,DM}}(\mathcal{L}) & \Psi_{22}^{\mathrm{CM,DM}}(\mathcal{L}) \end{bmatrix} \times \begin{bmatrix} V_{\mathrm{DM}}(\mathcal{L}) \\ I_{\mathrm{DM}}(\mathcal{L}) \end{bmatrix} \tag{53}$$

where

$$\begin{bmatrix} \Psi_{11}^{\mathrm{CM,DM}}(\mathcal{L}) & \Psi_{12}^{\mathrm{CM,DM}}(\mathcal{L}) \\ \Psi_{21}^{\mathrm{CM,DM}}(\mathcal{L}) & \Psi_{22}^{\mathrm{CM,DM}}(\mathcal{L}) \end{bmatrix} = \int_0^{\mathcal{L}} \mathbf{\Phi}_{\mathrm{CM}}(\mathcal{L}-z) \begin{bmatrix} -\Delta Z & 0 \\ 0 & -\Delta Y \end{bmatrix} \times \mathbf{\Phi}_{\mathrm{DM}}^{\mathrm{shift}}(z-\mathcal{L})\, dz \tag{54}$$

in which

$$\mathbf{\Phi}_{\mathrm{DM}}^{\mathrm{shift}}(\mathcal{L}) = \begin{bmatrix} -Z_{\mathrm{DM}_c}^{-1} \sinh \gamma_{\mathrm{DM}} \mathcal{L} & \cosh \gamma_{\mathrm{DM}} \mathcal{L} \\ \cosh \gamma_{\mathrm{DM}} \mathcal{L} & -Z_{\mathrm{DM}_c} \sinh \gamma_{\mathrm{DM}} \mathcal{L} \end{bmatrix} \tag{55}$$

Note that the closed expressions of $\Psi_{11}^{\mathrm{CM,DM}}(\mathcal{L})$, $\Psi_{12}^{\mathrm{CM,DM}}(\mathcal{L})$, $\Psi_{21}^{\mathrm{CM,DM}}(\mathcal{L})$, and $\Psi_{22}^{\mathrm{CM,DM}}(\mathcal{L})$ are given in appendix.

The induced CM currents at the input and output terminals due to DM-to-CM conversions are given as (56a)–(56c), shown at the bottom of the page.

For CM excitation, the input/output terminals are taken as

$$V_{\mathrm{DM}}(0) = -Z_{\mathrm{DM}_0} I_{\mathrm{DM}}(0) \tag{57a}$$
$$V_{\mathrm{DM}}(\mathcal{L}) = Z_{\mathrm{DM}_0} I_{\mathrm{DM}}(\mathcal{L}) \tag{57b}$$
$$V_{\mathrm{CM}}(0) = V_s - Z_{\mathrm{CM}_0} I_{\mathrm{CM}}(0) \tag{57c}$$
$$V_{\mathrm{CM}}(\mathcal{L}) = Z_{\mathrm{CM}_0} I_{\mathrm{CM}}(\mathcal{L}) \tag{57d}$$

By repeating the previous analysis, the total voltage and currents due to CM-to-DM conversion are given as

$$\begin{bmatrix} V_{\mathrm{DM,CM}} \\ I_{\mathrm{DM,CM}} \end{bmatrix} = \begin{bmatrix} \Psi_{11}^{\mathrm{DM,CM}}(\mathcal{L}) & \Psi_{12}^{\mathrm{DM,CM}}(\mathcal{L}) \\ \Psi_{21}^{\mathrm{DM,CM}}(\mathcal{L}) & \Psi_{22}^{\mathrm{DM,CM}}(\mathcal{L}) \end{bmatrix} \times \begin{bmatrix} V_{\mathrm{CM}}(\mathcal{L}) \\ I_{\mathrm{CM}}(\mathcal{L}) \end{bmatrix} \tag{58}$$

where $\Psi_{11}^{\mathrm{DM,CM}}(\mathcal{L}) = -\Psi_{22}^{\mathrm{CM,DM}}(\mathcal{L})$, $\Psi_{22}^{\mathrm{DM,CM}}(\mathcal{L}) = -\Psi_{11}^{\mathrm{CM,DM}}(\mathcal{L})$, $\Psi_{12}^{\mathrm{DM,CM}}(\mathcal{L}) = \Psi_{12}^{\mathrm{CM,DM}}(\mathcal{L})$, $\Psi_{21}^{\mathrm{DM,CM}}(\mathcal{L}) = \Psi_{21}^{\mathrm{CM,DM}}(\mathcal{L})$ and

$$V_{\mathrm{CM}}(\mathcal{L}) = \frac{Z_{\mathrm{CM}_c} Z_{\mathrm{CM}_0}}{\Delta_{\mathrm{CM}}} V_s \tag{59a}$$

$$I_{\mathrm{CM}}(0) = Z_{\mathrm{CM}_c} \frac{V_{\mathrm{CM,DM}} - Z_{\mathrm{CM}_0} I_{\mathrm{CM,DM}}}{\Delta_{\mathrm{CM}}} \tag{56a}$$
$$I_{\mathrm{CM}}(\mathcal{L}) = Z_{\mathrm{DM}_c} \frac{\left(V_{\mathrm{CM,DM}} + Z_{\mathrm{CM}_0} I_{\mathrm{CM,DM}}\right) \cosh \gamma_{\mathrm{CM}} \mathcal{L} + \left(\frac{Z_{\mathrm{CM}_0}}{Z_{\mathrm{CM}_c}} V_{\mathrm{CM,DM}} + Z_{\mathrm{CM}_c} I_{\mathrm{CM,DM}} \right) \sinh \gamma_{\mathrm{CM}} \mathcal{L}}{\Delta_{\mathrm{CM}}} \tag{56b}$$
$$\Delta_{\mathrm{CM}} = 2 Z_{\mathrm{CM}_0} Z_{\mathrm{CM}_c} \cosh \gamma_{\mathrm{CM}} \mathcal{L} + \left(Z_{\mathrm{CM}_c}^2 + Z_{\mathrm{CM}_0}^2 \right) \sinh \gamma_{\mathrm{CM}} \mathcal{L} \tag{56c}$$

$$I_{\mathrm{CM}}(\mathcal{L}) = \frac{Z_{\mathrm{CM}_c}}{\Delta_{\mathrm{CM}}} V_s \tag{59b}$$

Therefore, (60a) and (60b), as shown at the bottom of the page.

C. MIXED-MODE S-PARAMETERS

The mixed-mode S-parameters can be obtained from (46a)-(46d) by using the definition given in [33] and [34], hence

$$\begin{aligned} &s_{\mathrm{cc11}} \\ &= s_{\mathrm{cc22}} \\ &= \frac{\left(Z_{\mathrm{CM}_c}^2 - Z_{\mathrm{CM}_0}^2\right)\sinh\gamma_{\mathrm{CM}}\mathcal{L}}{2Z_{\mathrm{CM}_0}Z_{\mathrm{CM}_c}\cosh\gamma_{\mathrm{CM}}\mathcal{L} + \left(Z_{\mathrm{CM}_c}^2 + Z_{\mathrm{CM}_0}^2\right)\sinh\gamma_{\mathrm{CM}}\mathcal{L}} \end{aligned} \tag{61a}$$

$$\begin{aligned} &s_{\mathrm{cc21}} \\ &= s_{\mathrm{cc12}} \\ &= \frac{2Z_{\mathrm{CM}_0}Z_{\mathrm{CM}_c}}{2Z_{\mathrm{CM}_0}Z_{\mathrm{CM}_c}\cosh\gamma_{\mathrm{CM}}\mathcal{L} + \left(Z_{\mathrm{CM}_c}^2 + Z_{\mathrm{CM}_0}^2\right)\sinh\gamma_{\mathrm{CM}}\mathcal{L}} \end{aligned} \tag{61b}$$

$$\begin{aligned} &s_{\mathrm{dd11}} \\ &= s_{\mathrm{dd22}} \\ &= \frac{\left(Z_{\mathrm{DM}_c}^2 - Z_{\mathrm{DM}_0}^2\right)\sinh\gamma_{\mathrm{DM}}\mathcal{L}}{2Z_{\mathrm{DM}_0}Z_{\mathrm{DM}_c}\cosh\gamma_{\mathrm{DM}}\mathcal{L} + \left(Z_{\mathrm{DM}_c}^2 + Z_{\mathrm{DM}_0}^2\right)\sinh\gamma_{\mathrm{DM}}\mathcal{L}} \end{aligned} \tag{61c}$$

$$\begin{aligned} &s_{\mathrm{dd21}} \\ &= s_{\mathrm{dd12}} \\ &= \frac{2Z_{\mathrm{DM}_0}Z_{\mathrm{DM}_c}}{2Z_{\mathrm{DM}_0}Z_{\mathrm{DM}_c}\cosh\gamma_{\mathrm{DM}}\mathcal{L} + \left(Z_{\mathrm{DM}_c}^2 + Z_{\mathrm{DM}_0}^2\right)\sinh\gamma_{\mathrm{DM}}\mathcal{L}} \end{aligned} \tag{61d}$$

About the mixed-mode conversion parameters $\boldsymbol{S_{cd}}$ and $\boldsymbol{S_{dc}}$, their corresponding definition are used according to [33] and [34], hence,

$$s_{\mathrm{cd11}} = \frac{b_{\mathrm{c1}}}{a_{\mathrm{d1}}} = 2\frac{V_{\mathrm{CM}}(0) - Z_{\mathrm{CM}_0}I_{\mathrm{CM}}(0)}{V_{\mathrm{DM}}(0) + Z_{\mathrm{DM}_0}I_{\mathrm{DM}}(0)} \tag{62a}$$

$$s_{\mathrm{cd21}} = \frac{b_{\mathrm{c2}}}{a_{\mathrm{d1}}} = 2\frac{V_{\mathrm{CM}}(\mathcal{L}) + Z_{\mathrm{CM}_0}I_{\mathrm{CM}}(\mathcal{L})}{V_{\mathrm{DM}}(0) + Z_{\mathrm{DM}_0}I_{\mathrm{DM}}(0)} \tag{62b}$$

$$s_{\mathrm{dc11}} = \frac{b_{\mathrm{d1}}}{a_{\mathrm{c1}}} = \frac{1}{2}\frac{V_{\mathrm{DM}}(0) - Z_{\mathrm{DM}_0}I_{\mathrm{DM}}(0)}{V_{\mathrm{CM}}(0) + Z_{\mathrm{CM}_0}I_{\mathrm{CM}}(0)} \tag{62c}$$

$$s_{\mathrm{dc21}} = \frac{b_{\mathrm{d2}}}{a_{\mathrm{c1}}} = \frac{1}{2}\frac{V_{\mathrm{DM}}(\mathcal{L}) + Z_{\mathrm{DM}_0}I_{\mathrm{DM}}(\mathcal{L})}{V_{\mathrm{CM}}(0) + Z_{\mathrm{CM}_0}I_{\mathrm{CM}}(0)} \tag{62d}$$

By inserting Eqs. (49a)-(49b), (56a)-(56c), and (60a)-(60b), the following relations are obtained, *i.e.*

$$\begin{aligned} &s_{\mathrm{cd11}} \\ &= \frac{-2Z_0^2 Z_{\mathrm{DM}_c}Z_{\mathrm{CM}_c}}{\Delta_{\mathrm{DM}}\Delta_{\mathrm{CM}}}\left(2\Psi_{11}^{\mathrm{CM,DM}}(\mathcal{L}) - \frac{\Psi_{22}^{\mathrm{CM,DM}}(\mathcal{L})}{2}\right. \\ &\quad \left. + \frac{\Psi_{12}^{\mathrm{CM,DM}}(\mathcal{L})}{Z_0} - Z_0\Psi_{21}^{\mathrm{CM,DM}}(\mathcal{L})\right) \end{aligned} \tag{63a}$$

$$\begin{aligned} &s_{\mathrm{cd21}} \\ &= \frac{2Z_0^2 Z_{\mathrm{DM}_c}Z_{\mathrm{CM}_c}}{\Delta_{\mathrm{DM}}\Delta_{\mathrm{CM}}}\left[\left(2\Psi_{11}^{\mathrm{CM,DM}}(\mathcal{L}) + \frac{\Psi_{22}^{\mathrm{CM,DM}}(\mathcal{L})}{2}\right.\right. \\ &\quad \left. + \frac{\Psi_{12}^{\mathrm{CM,DM}}(\mathcal{L})}{Z_0} + Z_0\Psi_{21}^{\mathrm{CM,DM}}(\mathcal{L})\right)\cosh\gamma_{\mathrm{CM}}\mathcal{L} \\ &\quad + \left(\frac{Z_0}{Z_{\mathrm{CM}_c}}\Psi_{11}^{\mathrm{CM,DM}}(\mathcal{L}) + \frac{Z_{\mathrm{CM}_c}}{Z_0}\Psi_{22}^{\mathrm{CM,DM}}(\mathcal{L})\right. \\ &\quad \left.\left. + \frac{\Psi_{12}^{\mathrm{CM,DM}}(\mathcal{L})}{2Z_{\mathrm{CM}_c}} + 2Z_{\mathrm{CM}_c}\Psi_{21}^{\mathrm{CM,DM}}(\mathcal{L})\right)\sinh\gamma_{\mathrm{CM}}\mathcal{L}\right] \end{aligned} \tag{63b}$$

$$\begin{aligned} &s_{\mathrm{dc11}} \\ &= \frac{-2Z_0^2 Z_{\mathrm{DM}_c}Z_{\mathrm{CM}_c}}{\Delta_{\mathrm{DM}}\Delta_{\mathrm{CM}}}\left(\frac{\Psi_{11}^{\mathrm{DM,CM}}(\mathcal{L})}{2} - 2\Psi_{22}^{\mathrm{DM,CM}}(\mathcal{L})\right. \\ &\quad \left. + \frac{\Psi_{12}^{\mathrm{DM,CM}}(\mathcal{L})}{Z_0} - Z_0\Psi_{21}^{\mathrm{DM,CM}}(\mathcal{L})\right) \end{aligned} \tag{63c}$$

$$\begin{aligned} &s_{\mathrm{dc21}} \\ &= \frac{2Z_0^2 Z_{\mathrm{DM}_c}Z_{\mathrm{CM}_c}}{\Delta_{\mathrm{DM}}\Delta_{\mathrm{CM}}}\left[\left(\frac{\Psi_{11}^{\mathrm{DM,CM}}(\mathcal{L})}{2} + 2\Psi_{22}^{\mathrm{DM,CM}}(\mathcal{L})\right.\right. \\ &\quad \left. + \frac{\Psi_{12}^{\mathrm{DM,CM}}(\mathcal{L})}{Z_0} + Z_0\Psi_{21}^{\mathrm{DM,CM}}(\mathcal{L})\right)\cosh\gamma_{\mathrm{DM}}\mathcal{L} \\ &\quad + \left(\frac{Z_0}{Z_{\mathrm{DM}_c}}\Psi_{11}^{\mathrm{DM,CM}}(\mathcal{L}) + \frac{Z_{\mathrm{DM}_c}}{Z_0}\Psi_{22}^{\mathrm{DM,CM}}(\mathcal{L})\right. \\ &\quad \left.\left. + \frac{2\Psi_{12}^{\mathrm{DM,CM}}(\mathcal{L})}{Z_{\mathrm{DM}_c}} + Z_{\mathrm{DM}_c}\frac{\Psi_{21}^{\mathrm{DM,CM}}(\mathcal{L})}{2}\right)\sinh\gamma_{\mathrm{DM}}\mathcal{L}\right] \end{aligned} \tag{63d}$$

After performing some algebra simplifications, it can be deduced that $s_{\mathrm{cd11}} = s_{\mathrm{dc11}}$ and $s_{\mathrm{cd21}} = s_{\mathrm{dc21}}$.

V. COMPUTED RESULTS AND VALIDATION

In this section, the proposed model of high-speed cable is validated by making a comparison with FEKO/HFSS software. Three different cable geometries have been considered, as shown in Fig. 11. The parameters of the cable are taken

$$I_{\mathrm{DM}}(0) = Z_{\mathrm{DM}_c}\frac{V_{\mathrm{DM,CM}} - Z_{\mathrm{DM}_0}I_{\mathrm{DM,CM}}}{\Delta_{\mathrm{DM}}} \tag{60a}$$

$$I_{\mathrm{DM}}(\mathcal{L}) = Z_{\mathrm{DM}_c}\frac{\left(V_{\mathrm{DM,CM}} + Z_{\mathrm{DM}_0}I_{\mathrm{DM,CM}}\right)\cosh\gamma_{\mathrm{DM}}\mathcal{L} + \left(\frac{Z_{\mathrm{DM}_0}}{Z_{\mathrm{DM}_c}}V_{\mathrm{DM,CM}} + Z_{\mathrm{DM}_c}I_{\mathrm{DM,CM}}\right)\sinh\gamma_{\mathrm{DM}}\mathcal{L}}{\Delta_{\mathrm{DM}}} \tag{60b}$$

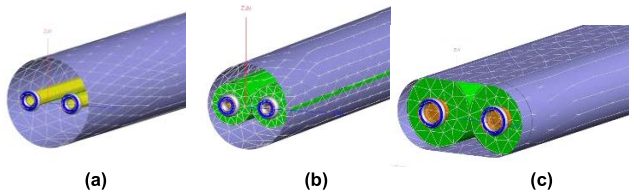

FIGURE 11. Different high-speed cable geometries. (a) Circular shield without the dielectric. (b) Circular shield with lossy dialectic. (c) Oval-shaped shield with lossy dielectric.

as $r_w = 0.2675$ mm, $r_{\text{sh}} = s = 1.56$ mm, $t = 9\ \mu$m, and the total length of the cable is taken as $\mathcal{L} = 0.2\ m$. The inner conductors are assumed to be copper material and the outer shield is considered to be aluminum, whereas the dielectric material is considered to be Fluorinated ethylene propylene (FEP), which has a relative permittivity $\epsilon_r = 2$ and dielectric loss tangent $\tan\delta_{\text{Loss}} = 5 \times 10^{-4}$. It is worth noticing that the length of the cable is taken to be short in order to reduce the FEKO/HFSS software simulation time, which would be unreasonable for a cable with a higher length. About the FEKO model, the mesh "**Coarse**" is selected in order to achieve a tradeoff between accuracy and simulation time+ memory resources. Also, the edge ports are used in cut cylinders which represent the conductors, where perfectly electric conductor flats are used at the terminals to avoid any undesired radiations from the ports. About the HFSS model, the wave ports are used to avoid radiations, where a default mesh is selected to reduce simulation time.

It is seen that for the arbitrary shape as shown in Fig. 11 (c) the p.u.l parameters are computed numerically where the skin and proximity effects can be still used using equivalent circles.

It can be observed from Fig. 12 that a good agreement is obtained between the proposed model and the results of software FEKO and HFSS for case (a), Fig. 11. For the high-speed cable with a lossy dielectric as shown in Fig. 13, a good agreement is also obtained. However, with some slight discrepancies are observed with the high-speed cable that has an oval-shaped shield. Moreover, the stranger behavior of the FEKO plots, which show some resonance peaks are only observable, when a lossy dielectric is introduced into the cable. this is due to the unstable solutions at that specific frequency points. This is because we do not activate the low frequency stabilization so as to avoid lengthening the simulation time. Also, the mesh is not in its standard sense, which also can generate some errors in the MoM solver.

To study the LCL and TCL in the high-speed cable, slightly unbalanced cables are implemented. In the first case, a shield deformation is considered, i.e., the outer shield is not smooth, but it has a narrow longitudinal slot, which models the nature of the actual shield, which is usually folded around the coated conductors. This idea was proposed in [9] so as to study the spiral shield. Here, it will be applied to study the effect of the irregularities of the foil shield. The p.u.l transfer impedance and admittance of a longitudinal

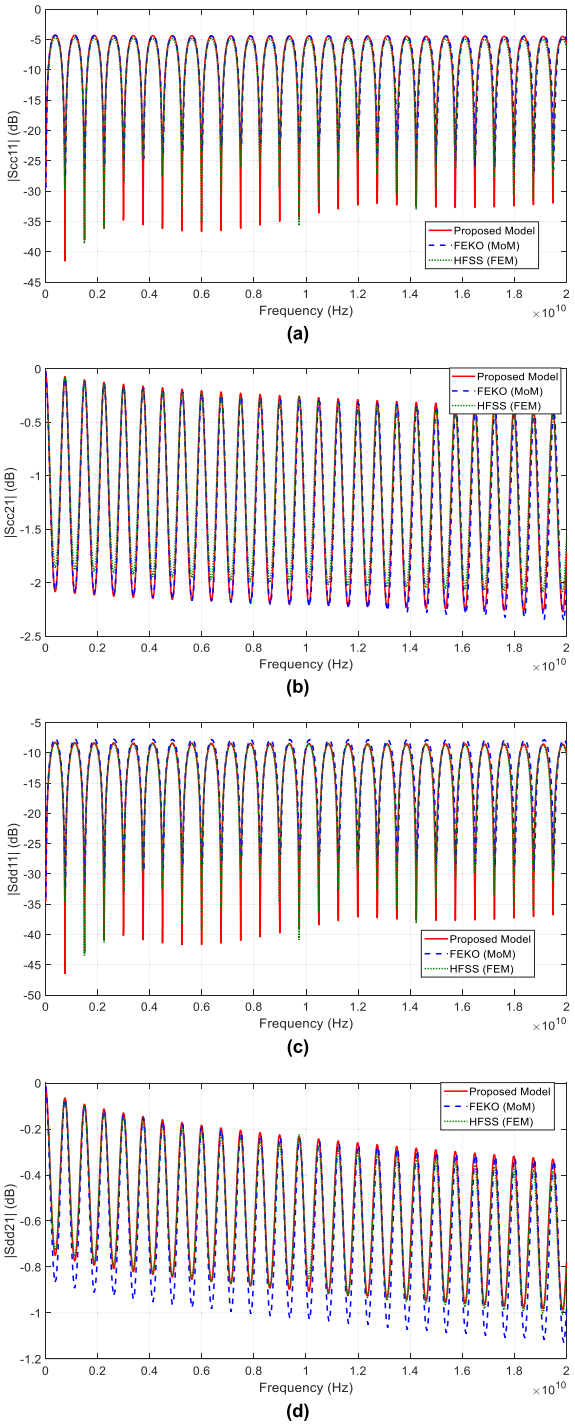

FIGURE 12. The magnitude of the mixed-mode S-parameters of a high-speed cable with circular shield and without dielectric (case (a), Fig. 11).

slot can be obtained as [20] and [21]

$$L_{\text{slot}}(\alpha,\phi) = \frac{\mu_0}{\pi}\left(\frac{d}{4r_{sh}}\right)^2 \Pi_\phi(\alpha)^2 \tag{64a}$$

$$C_{\text{slot}}(\alpha,\phi) = \frac{\epsilon_{\text{eq}}}{\pi}\left(\frac{d}{4r_{sh}N}\right)^2 \Pi_\phi(\alpha)^2 \tag{64b}$$

where $N = \frac{1}{4\pi^2 D^2}$ and d is the slot width. Hence, the p.u.l inductance and capacitance of the high-speed cable are modified as [20]

$$\boldsymbol{L}_a = \boldsymbol{L} + \text{diag}\left(L_{\text{slot}}\left(\alpha, 0\right), L_{\text{slot}}\left(\alpha, \pi\right)\right) \quad (65a)$$

$$\boldsymbol{C}_a = \boldsymbol{C} - \text{diag}\left(C_{\text{slot}}\left(\alpha, 0\right), C_{\text{slot}}\left(\alpha, \pi\right)\right) \quad (65b)$$

in which the "diag" operation represents the diagonal matrix.

In the second case, the positions of the inner coated conductors are considered to be unsymmetrically located with respect to the central axis of the cable so as to emulate the disturbances and irregularities during the fabrication process. It means that $\mathcal{Z}_{1/2} = \frac{s}{2}(1 \pm \delta\mathcal{Z}_{1/2})$, in which $\delta\mathcal{Z}_{1/2}$ represent the effect of irregularities between the inner conductors of the high-speed cable.

The results for a high-speed cable with a longitudinal slot are presented in Fig. 14, whereas the results of high-speed cable with unsymmetrically located conductors are shown in Fig. 15.

It can be observed from Fig. 14, that good results are obtained with some discrepancies between the proposed model and commercial software. This is due to the limitation of our proposed model. Also, it can be seen that the results of HFSS and FEKO software do not match because the conversion parameters S_{cd} of a balanced transmission line with slight shield deformation are very small in magnitude and sensitive to any small variation in the parameters, hence, it is very hard to predict. However, for a high-speed cable with unsymmetrically located conductors, very good agreements are obtained, as shown in Figs. 15 (a) and (b). this is due to the fact that the conversions between CM and DM signals are high and can be predicted very easily. Consequently, it can be deduced that any slight unbalances in the high-speed cable can cause conversions between the modes which can deteriorate the transmitted signal. It is worth noticing that S_{cd21} has a high magnitude in high-speed cable with a lossy dielectric as compared to the one without dielectric, as shown in Figs. 15 (a) and (b). This is due to the fact that the existence of the dielectric in a high-speed cable with unsymmetrically located inner conductors can cause higher unbalanced geometry in the cross-section of the cable.

Moreover, it should be indicated that our method is programmed in MATLAB, then it is executed in a laptop computer with processor Intel(R) Core(TM) i7-8550U CPU @ 1.80 GHz equipped with 8 GB RAM. The simulation time takes only a fraction of second with memory usage less than 1 GB for any cable length. Whereas, the FEKO simulations are executed in a server computer with two processors intel (R), Xeon (R) Gold 6152 CPU @ 2.1 GHz equipped with 521 GB RAM. The simulation time is 133.2 hours (5.5 days) with memory usage 57.24 GB for cable with oval shaped shield and has length 0.2 m. Consequently, it is apparent that our method has good advantages as compared to full-wave methods, also it gives us a good insight about the physical concepts such as skin effect in high-speed cable systems.

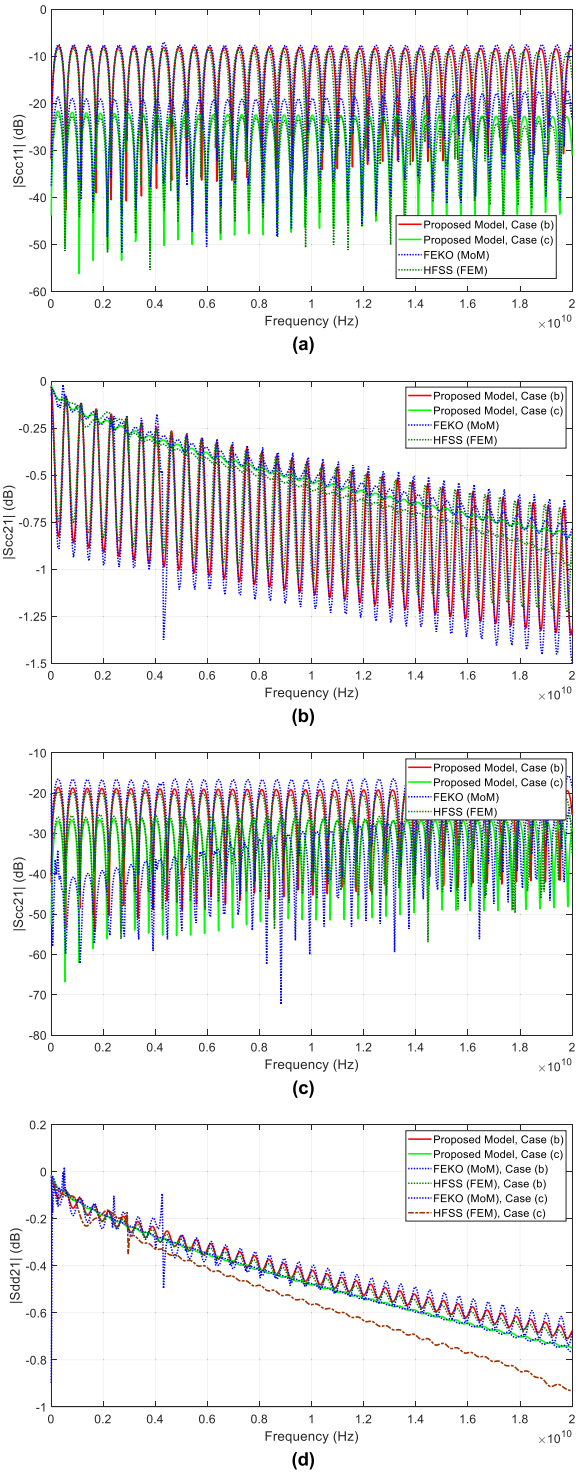

FIGURE 13. The magnitude of the mixed-mode S-parameters of a high-speed cable with circular shield Circular shield with lossy dialectic (case (b) and (c), Fig. 11).

VI. EXPERIMENTAL RESULTS

In this section, an experiment is carried out to further validate the proposed model. The measurement setup is shown in Fig. 16, where a vector network analyzer (VNA) is used with the raw cable 20 GHz fixtures. It is worth mentioning

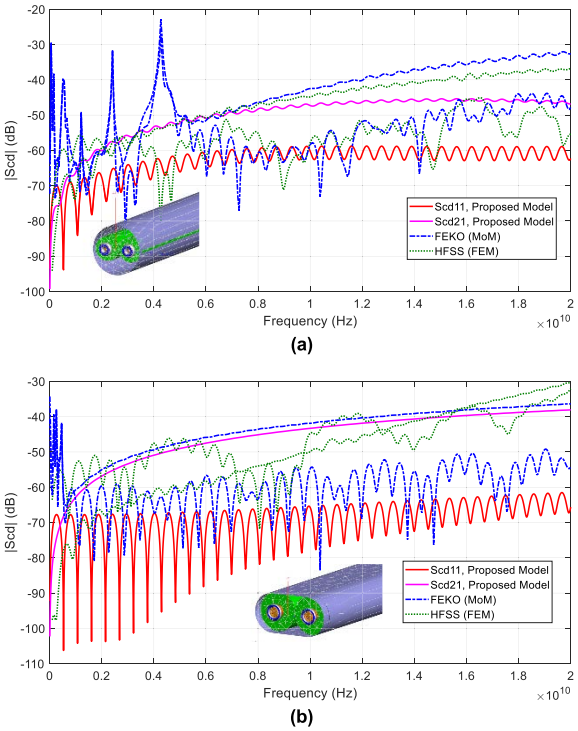

FIGURE 14. The DM-to-CM conversion parameters of the high-speed cable with longitudinal a slot along its shield with $d = 0.05$ mm. (a) Circular shield with lossy dialectric. (b) Oval shaped shield with lossy dielectric.

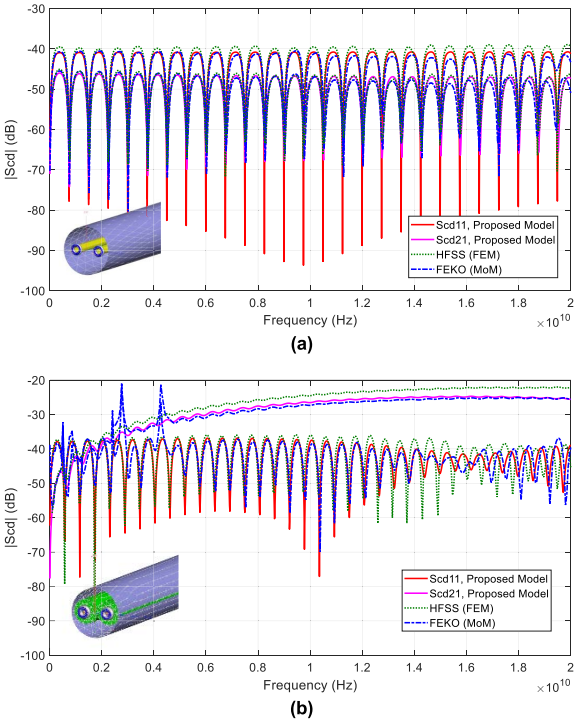

FIGURE 15. The DM-to-CM conversion parameters of the high-speed cable with unsymmetrically located conductors with $\delta\mathcal{Z}_1 = 0.05r_{sh}/2$ and $\delta\mathcal{Z}_2 = 0$. (a) Circular shield without the dielectric. (b) Circular shield with lossy dialectric.

that the fixtures are used in order to connect the 26AWG high-speed cable with the VNA cables. However, these fixtures have a nonnegligible effect on the measured mixed-mode S-parameters of the cable [35], [36]. It means that the measured mixed-mode S-parameters are actually representing the system of the cable embedded with the two fixtures. It is worth noticing that the fixtures consist of a well-balanced printed circuit board (PCB) inside a metallic

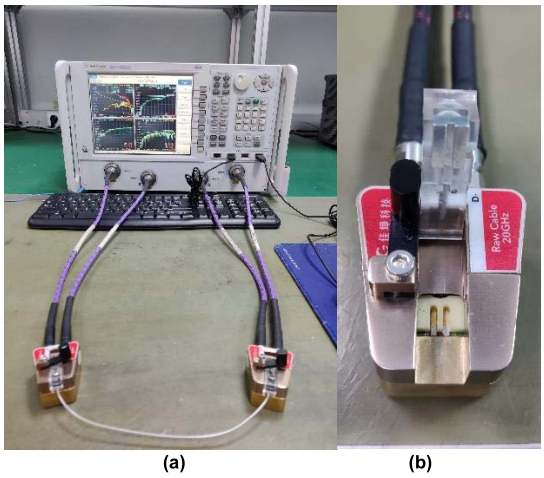

FIGURE 16. Measuring instruments. (a) measuring setup. (b) fixture.

TABLE 1. Parameters of 26AWG high-speed cable.

Parameters	Values
Signal wire diameter (copper)	0.415 mm
Drain wire diameter (copper)	0.400 mm
Wire insulation diameter (FEP)	1.42 mm
Shield layer thickness (AL)	0.009 mm

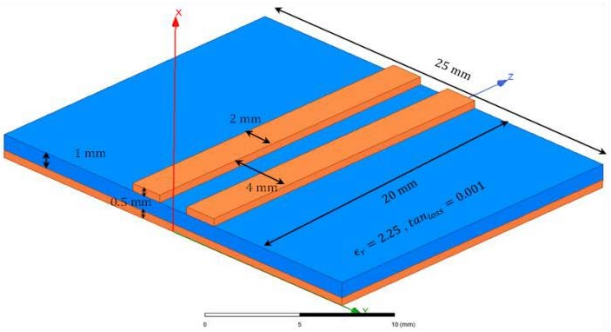

FIGURE 17. The designed PCB in HFSS software to model the effect of the fixtures during the measurement process (the traces and the ground are copper material).

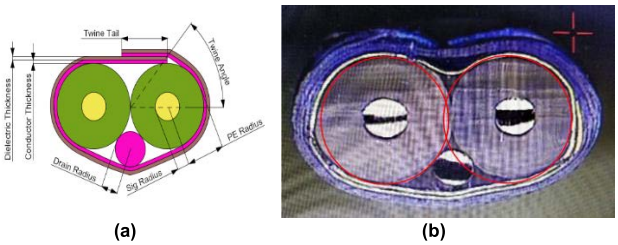

FIGURE 18. Cross-section of 26AWG high-speed cable. (a) sketched. (b) Real zoomed view. The two red circles with the same radius show the unbalance of the real fabricated highspeed cable.

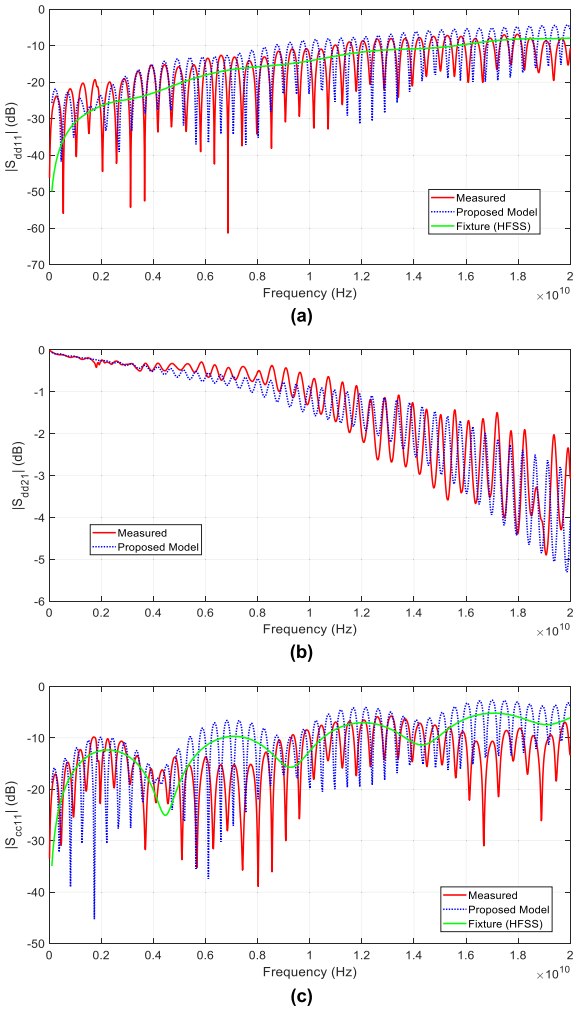

FIGURE 19. The magnitude of the mixed-mode S-parameters of 26AWG high-speed cable.

enclosure, as shown in Fig. 16. To include the effect of the fixtures in our proposed model, a simplified model for the fixture is designed in the HFSS software as shown in Fig. 17, and then its S-parameters are extracted and cascaded with the S-parameters of the highspeed cable [36]. A 26AWG cable fabricated in the Zhaolong company is used, and its parameters are summarized in table 1, and its cross-section is shown in Fig. 18. The comparison between the proposed model cascaded with fixture effects and the measured results of 26AWG highspeed cable with 0.2 m length are shown in Figs. 19 and 20. It can be observed that a good agreement is obtained between the proposed model and the measurement results. However, the envelope difference in the S_{cc11} parameter between the model and the measurement results is only due to the effect of the actual fixture, which has different S_{cc11} from the one that we have designed in HFSS. Note that the envelope of S_{dd11} and S_{cc11} represent the S_{dd11} and S_{cc11} of the fixture as shown in Figs 19 (a) and (c), respectively.

Moreover, it can be seen from Fig. 20 that the TCL parameters of a perfectly balanced cable are relatively small as compared to the measured one. However, if we consider

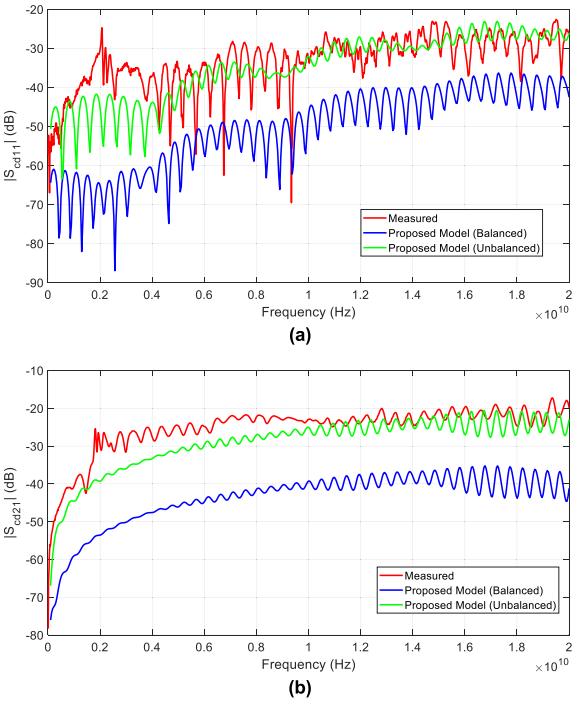

FIGURE 20. The magnitude of the TCL parameters of 26AWG high-speed cable, where the unbalanced cable has one of the inner conductors shifted by 5 % from its original position.

slightly unbalanced cable, the level of the TCL parameters increases, and good agreement is obtained because, in fact, the actual fabricated cables are not perfectly balanced, and higher conversions between modes have been occurred. This due to the fact that the real fabricated highspeed cables have many deformations that cannot be avoided due to the uncertainties during the fabrication process. We have plotted two circles with exactly the same radius as shown in Fig. 18. It can be observed that there are many different deformations in the fabricated cable. a) deformation in the shield b) deformation in the dielectric. c) deformation in the location of the wires. To model this deformation we have, considered 5% shift of one of the inner conductors.

VII. CONCLUSION

In this paper, an efficient transmission line model of high-speed cables has been developed to predict its response at high-frequency ranges up to 20 GHz. To do that, accurate modeling of the p.u.l parameters has been established, and the skin and proximity effect of the conductors and shield have been formulated in the closed-form. Consequently, the mixed-mode S-parameters of the highspeed cables have been generated, and the conversions between the CM and DM signals have been investigated in detail. It has been shown that any slight unbalances in the highspeed cable can cause high conversions between the modes, which can deteriorate the transmitted signal. The obtained results have been compared with measurement one, and very good agreement has been obtained, and it has been shown that the S-parameters of the cable are critical and can be affected by the measuring instruments.

APPENDIX

The expressions of $\Psi_{11}^{\mathrm{CM,DM}}(\mathcal{L})$, $\Psi_{12}^{\mathrm{CM,DM}}(\mathcal{L})$, $\Psi_{21}^{\mathrm{CM,DM}}(\mathcal{L})$, and $\Psi_{22}^{\mathrm{CM,DM}}(\mathcal{L})$ are derived as

$$\begin{aligned}\Psi_{11}^{\mathrm{CM,DM}}(\mathcal{L}) &= \frac{-\frac{\Delta Z}{Z_{\mathrm{DM}_c}}+\Delta Y Z_{\mathrm{CM}_c}}{2(\gamma_{\mathrm{DM}}+\gamma_{\mathrm{CM}})}\left(\cosh(\gamma_{\mathrm{DM}}+\gamma_{\mathrm{CM}})\mathcal{L}-1\right)\\ &\quad-\frac{\frac{\Delta Z}{Z_{\mathrm{DM}_c}}+\Delta Y Z_{\mathrm{CM}_c}}{2(\gamma_{\mathrm{DM}}-\gamma_{\mathrm{CM}})}\left(\cosh(\gamma_{\mathrm{DM}}-\gamma_{\mathrm{CM}})\mathcal{L}-1\right)\end{aligned} \tag{A1}$$

$$\begin{aligned}\Psi_{12}^{\mathrm{CM,DM}}(\mathcal{L}) &= \frac{-\Delta Z+\Delta Y Z_{\mathrm{CM}_c}Z_{\mathrm{DM}_c}}{2(\gamma_{\mathrm{DM}}+\gamma_{\mathrm{CM}})}\sinh(\gamma_{\mathrm{DM}}+\gamma_{\mathrm{CM}})\mathcal{L}\\ &\quad-\frac{\Delta Z+\Delta Y Z_{\mathrm{CM}_c}Z_{\mathrm{DM}_c}}{2(\gamma_{\mathrm{DM}}-\gamma_{\mathrm{CM}})}\sinh(\gamma_{\mathrm{DM}}-\gamma_{\mathrm{CM}})\mathcal{L}\end{aligned} \tag{A2}$$

$$\begin{aligned}\Psi_{21}^{\mathrm{CM,DM}}(\mathcal{L}) &= \frac{\frac{\Delta Z}{Z_{\mathrm{CM}_c}Z_{\mathrm{DM}_c}}-\Delta Y}{2(\gamma_{\mathrm{DM}}+\gamma_{\mathrm{CM}})}\sinh(\gamma_{\mathrm{DM}}+\gamma_{\mathrm{CM}})\mathcal{L}\\ &\quad-\frac{\frac{\Delta Z}{Z_{\mathrm{CM}_c}Z_{\mathrm{DM}_c}}+\Delta Y}{2(\gamma_{\mathrm{DM}}-\gamma_{\mathrm{CM}})}\sinh(\gamma_{\mathrm{DM}}-\gamma_{\mathrm{CM}})\mathcal{L}\end{aligned} \tag{A3}$$

$$\begin{aligned}\Psi_{22}^{\mathrm{CM,DM}}(\mathcal{L}) &= \frac{\frac{\Delta Z}{Z_{\mathrm{CM}_c}}-\Delta Y Z_{\mathrm{DM}_c}}{2(\gamma_{\mathrm{DM}}+\gamma_{\mathrm{CM}})}\left(\cosh(\gamma_{\mathrm{DM}}+\gamma_{\mathrm{CM}})\mathcal{L}-1\right)\\ &\quad-\frac{\frac{\Delta Z}{Z_{\mathrm{CM}_c}}+\Delta Y Z_{\mathrm{DM}_c}}{2(\gamma_{\mathrm{DM}}-\gamma_{\mathrm{CM}})}\left(\cosh(\gamma_{\mathrm{DM}}-\gamma_{\mathrm{CM}})\mathcal{L}-1\right)\end{aligned} \tag{A4}$$

REFERENCES

[1] *IEEE Standards for Local Area Networks: Carrier Sense Multiple Access With Collision Detection (CSMA/CD) Access Method and Physical Layer Specifications*, Standard 802.3–1985, ANSI/IEEE, 1985.

[2] *IEEE Standard for Local and Metropolitan Area Networks—System Considerations for Multi-Segment 10 Mb/S Baseband Networks (Section 13) and Twisted-Pair Medium Attachment Unit (MAU) and Baseband Medium, Type 10BASE-T (Section 14)*, Standard 802.3i-1990 (Supplement to ISO/IEC 8802-3:1990—ANSI/IEEE Std 802.3–1990 Edition), IEEE, Dec. 1990, pp. 1–66.

[3] *IEEE Standard for Information Technology—Telecommunications and Information Exchange Between Systems—Local and Metropolitan Area Networks—Part 3: Carrier Sense Multiple Access With Collision Detection (CSMA/CD) Access Method and Physical Layer Specifications—Physical Layer Parameters and Specifications for 1000 Mb/s Operation Over 4 Pair of Category 5 Balanced Copper Cabling, Type 1000BASE-T*, Standard 802.3ab-1999, IEEE, Jul. 1999, pp. 1–144.

[4] *IEEE Standard for Information Technology—Local and Metropolitan Area Networks—Part 3: CSMA/CD Access Method and Physical Layer Specifications Amendment: Physical Layer and Management Parameters for 10 Gb/s Operation, Type 10GBASE-CX4*, Standard 802.3ak-2004 (Amendment to IEEE Std 802.3–2002 as amended by IEEE Stds 802.3ae-2002, 802.3af-2003 and 802.3aj-2003), IEEE, Mar. 2004, pp. 1–56.

[5] IEEE 802.3 Ethernet Working Group. (Aug. 22, 2022). *IEEE 802.3 Ethernet*. Accessed: Sep. 21, 2022. [Online]. Available: https://www.ieee802.org/3

[6] *IEEE P802.3ckTM/D1.5 Draft Standard for Ethernet Amendment: Physical Layer Specifications and Management Parameters for 100 Gb/s, 200 Gb/s, and 400 Gb/s Electrical Interfaces Based on 100 Gb/s Signaling*, Standard IEEE P802.3ck/D1.5, Mar. 2021.

[7] T. Sugiyama, H. Nonen, I. Fukasaku, H. Ishikawa, and T. Kumakura, "High-speed transmission copper cable for 25 Gbit/s/lane," in *Proc. 3rd IEEE CPMT Symp. Jpn.*, Nov. 2013, pp. 1–4.

[8] D. N. de Araujo, M. Commens, B. Mutnury, and J. Diepenbrock, "TwinAx differential cable helical shield wrap modeling," in *Proc. IEEE Electr. Perform. Electron. Packag.*, Oct. 2007, pp. 299–302.

[9] D. N. de Araujo, G. Pitner, M. Commens, B. Mutnury, and J. Diepenbrock, "Full-wave, TwinAx, differential cable modeling," in *Proc. 58th Electron. Compon. Technol. Conf.*, May 2008, pp. 1684–1689.

[10] (2020). *ANSYS Electromagnetic Suite 2020 R1*. HFSS Help. ANASYS, Inc. Southpointe 2600 ANSYS Drive Canonsburg, PA, USA. [Online]. Available: https://www.ansys.com

[11] Z. Chen, M. Prasad, D. O'Connor, P. Bond, and A. Muszynski, "Differential twinax cable modeling by measured 4-port S-parameters," in *Proc. IEEE 14th Topical Meeting Electr. Perform. Electron. Packag.*, Oct. 2005, pp. 87–90.

[12] D.-C. Chang, H.-B. Liang, J.-R. Wang, V. Chen, J.-P. Zhang, and Y.-S. Lin, "High dip insertion loss due to periodic defect structure in high speed transmission line," in *Proc. Asia–Pacific Symp. Electromagn. Compat. (APEMC)*, May 2015, pp. 494–497.

[13] S. Mortazavi, D. Schleicher, A. Stieler, A. Sinai, F. Gerfers, and M. Hampe, "EMC analysis of shielded twisted pair and shielded parallel pair transmission lines for automotive multi-gig Ethernet," in *Proc. IEEE Int. Symp. Electromagn. Compat., Signal Power Integrity (EMC+SIPI)*, Jul. 2019, pp. 193–198.

[14] B. Nouri, M. S. Nakhla, and R. Achar, "Efficient simulation of nonlinear transmission lines via model-order reduction," *IEEE Trans. Microw. Theory Techn.*, vol. 65, no. 3, pp. 673–683, Mar. 2017.

[15] B. Nouri and M. S. Nakhla, "Model order reduction of nonlinear transmission lines using interpolatory proper orthogonal decomposition," *IEEE Trans. Microw. Theory Techn.*, vol. 66, no. 12, pp. 5429–5438, Dec. 2018.

[16] J. Muñoz-Enano, P. Vélez, and F. Martín, "Signal balancing in unbalanced transmission lines," *IEEE Trans. Microw. Theory Techn.*, vol. 67, no. 8, pp. 3339–3349, Aug. 2019.

[17] Q. Chen, F. Ghasemifard, G. Valerio, and O. Quevedo-Teruel, "Modeling and dispersion analysis of coaxial lines with higher symmetries," *IEEE Trans. Microw. Theory Techn.*, vol. 66, no. 10, pp. 4338–4345, Oct. 2018.

[18] D. M. Cortés-Hernández, R. J. Sánchez-Mesa, S. C. Sejas-García, and R. Torres-Torres, "Extraction of frequency-dependent characteristic impedance and complex permittivity in single-ended and edge-coupled transmission lines using the calculated series parasitic effects," *IEEE Trans. Microw. Theory Techn.*, vol. 65, no. 9, pp. 3116–3122, Sep. 2017.

[19] C.-C. Huang, "Determination of characteristic impedance of planar transmission lines on lossy/dispersive substrates by using series resistor with frequency-dependent inductance," *IEEE Trans. Microw. Theory Techn.*, vol. 68, no. 10, pp. 4229–4235, Oct. 2020.

[20] O. Gassab, S. Bouguerra, L. Zhou, and W.-Y. Yin, "Efficient analytical model for the transfer impedance and admittance of noncoaxial/twinax braided–shielded cables," *IEEE Trans. Electromagn. Compat.*, vol. 62, no. 6, pp. 2725–2736, Dec. 2020.

[21] K. S. H. Lee and C. E. Baum, "Application of modal analysis to braided-shield cables," *IEEE Trans. Electromagn. Compat.*, vol. EMC-17, no. 3, pp. 159–169, Aug. 1975.

[22] N. Marcuvitz, *Waveguide Handbook*, vol. 10. New York, NY, USA: McGraw-Hill, 1951.

[23] C. R. Paul, *Analysis of Multiconductor Transmission Lines*. New York, NY, USA: Wiley, 1994.

[24] S. A. Schelkunoff, "The electromagnetic theory of coaxial transmission lines and cylindrical shields," *Bell Syst. Tech. J.*, vol. 13, no. 4, pp. 532–579, Oct. 1934.

[25] M. Zhang, J. Liu, L. Liao, H. Gao, D. Zhu, F. Zhuo, and P. Qi, "A calculation method on high-frequency loss of double-layer composite conductor," *IEEE Trans. Electromagn. Compat.*, vol. 60, no. 3, pp. 647–656, Jun. 2018.

[26] C. A. Balanis, *Advanced Engineering Electromagnetics*. Hoboken, NJ, USA: Wiley, 1999.

[27] D. A. Frickey, "Conversions between S, Z, Y, H, ABCD, and T parameters which are valid for complex source and load impedances," *IEEE Trans. Microw. Theory Techn.*, vol. 42, no. 2, pp. 205–211, Feb. 1994.

[28] S. Vujević, D. Lovrić, and V. Boras, "High-accurate numerical computation of internal impedance of cylindrical conductors for complex arguments of arbitrary magnitude," *IEEE Trans. Electromagn. Compat.*, vol. 56, no. 6, pp. 1431–1438, Dec. 2014.

[29] (2019). COMSOL AB. *COMSOL Multiphysics 5.5 Reference Manual*. Burlington, MA, USA. [Online]. Available: https://www.comsol.com

[30] (2019). *Altair FEKO 2019.3.3 User's Manual*. EM Software and Systems, S. A. (Pty) Ltd. Stellenbosch, South Africa. [Online]. Available: https://www.feko.info

[31] F. Grassi, Y. Yang, X. Wu, G. Spadacini, and S. A. Pignari, "On mode conversion in geometrically unbalanced differential lines and its analogy with crosstalk," *IEEE Trans. Electromagn. Compat.*, vol. 57, no. 2, pp. 283–291, Apr. 2015.
[32] F. Grassi, P. Manfredi, X. Liu, J. Sun, X. Wu, D. V. Ginste, and S. A. Pignari, "Effects of undesired asymmetries and nonuniformities in differential lines," *IEEE Trans. Electromagn. Compat.*, vol. 59, no. 5, pp. 1613–1624, Oct. 2017.
[33] W. Fan, A. Lu, L. L. Wai, and B. K. Lok, "Mixed-mode S-parameter characterization of differential structures," in *Proc. 5th Electron. Packag. Technol. Conf. (EPTC)*, Dec. 2003, pp. 533–537.
[34] A. Huynh, M. Karlsson, and S. Gong, "Mixed-mode S-parameters and conversion techniques," in *Advanced Microwave Circuits and Systems*, V. Zhurbenko, Ed. London, U.K.: IntechOpen, 2010. [Online]. Available: https://www.intechopen.com/chapters/9636, doi: 10.5772/8419.
[35] X. Ye, "De-embedding errors due to inaccurate test fixture characterization," *IEEE Electromagn. Compat. Mag.*, vol. 1, no. 4, pp. 75–78, 4th Quart., 2012.
[36] "The ABCs of de-embedding," Agilent Technol., Santa Clara, CA, USA, Agilent Appl. Note 5989-5765EN, Jun. 2007.

OUSSAMA GASSAB (Member, IEEE) was born in Djelfa, Algeria. He received the B.Sc. degree in electrical and electronic engineering and the M.Sc. degree in telecommunications from the National Institute of Electrical and Electronic Engineering (IGEE), Boumerdes, Algeria, in 2013 and 2015, respectively, and the Ph.D. degree in electrical engineering about electromagnetic compatibility (EMC) from Shanghai Jiao Tong University, Shanghai, China, in 2020.

He is currently a Postdoctoral Research Fellow with the Department of Information Science and Electronic Engineering, Zhejiang University, Hangzhou, China. His research interests include electromagnetic compatibility, antenna array design, distributed-parameter circuit modeling, statistical models for the characterization of interference effects, high speed cable modeling, and shielding effectiveness. He is also interested in the fields of power electronics, mathematics, and modern physics.

YANNING CHEN received the B.S. degree in computer science from Capital Normal University, in 2002, and the M.S. degree in electronic and communication engineering from the Beijing University of Posts and Telecommunications, in 2018. She is currently a Senior Engineer, the Vice Director of the Chip Laboratory, and the Executive Director of the Beijing Chip Identification Technology Company, Ltd. She has long been engaged in industrial chip design and generic technology research. She led the team to study the application environment of power industry chips, formulate relevant technical standards, and establish the quality assurance system of industrial chips.

YALI SHAO received the B.S. and M.S. degrees in electronic engineering from Zhejiang University, Hangzhou, China, in 2008 and 2011, respectively.

She was at Texas Instruments, from 2011 to 2017; and then at Beijing Smart-Chip Microelectronics Technology Company Ltd.1 (analog devices), from 2017 to 2021. She was the expert of the Analog Design and Analog/Mixed-Signal Design Verification. She has been with the Beijing Xin Kejian Technology, since 2021. Her current research interests include process and device TCAD EDA, analog mixed-signal design automation EDA, and analog IC design (power IC, driver IC, isolation IC, and ADC IC).

JINGXIAO LI was born in Zhejiang, China. She received the B.E. degree in network engineering from the University of Electronic Science and Technology of China, Chengdu, in 2019, and the master's degree in electronics and communication engineering from Zhejiang University, Hangzhou, China, in March 2022. Her research interests include electromagnetic compatibility (EMC), high speed cable modeling and design, distributed-parameter circuit modeling, field-to-wire coupling, near field modeling, statistical analysis of interference effects, and shielding effectiveness.

DING-E WEN received the M.S. degree in theoretical physics from Central China Normal University, Wuhan, China, in 2004, and the Ph.D. degree in electromagnetic field and microwave technology from Southeast University, Nanjing, in 2014. She is currently an Engineer with the Science and Technology on Electromagnetic Compatibility Laboratory. Her current research interests include electromagnetic numerical computation and electromagnetic scattering.

FANG HE (Senior Member, IEEE) received the B.Eng. degree in communication engineering from Jilin University, Changchun, China, in 2002, and the M.Sc. degree in communication engineering and the Ph.D. degree in electrical and electronics engineering from the University of Manchester, Manchester, U.K., in 2005 and 2011, respectively.

He has been with HellermannTyton Data Ltd., Northampton, U.K., since 2009, where he was the Product Development Engineer. Since 2019, he has been with Zhejiang Zhaolong Interconnect Technology Company Ltd., Deqing, China, where he is the Chief Specialist of Generic Cabling and the Laboratory Director.

Dr. He is a member of Institution of Engineering and Technology (IET), U.K. He is also a Chartered Engineer from the Engineering Council, U.K.

ZHIZHEN SU received the B.S. degree in communication engineering from Lanzhou Jiaotong University, Lanzhou, China, in 2014. He is currently pursuing the M.S. degree in electronic science and technology with Zhejiang University, Hangzhou, China.

His research interests include electromagnetic compatibility, high-speed cable modeling and design, and machine learning.

PEINA ZHONG received the bachelor's degree from the Hunan Institute of Engineering, Xiangtan, China, in 2013.

She started engineering career at the Hangzhou Applied Acoustics Research Institute, Hangzhou (CSIC 715th Marine Institute), from 2013 to 2022, and get the National Professional and Technical Cadre Qualification as an Engineer, in 2018. While get involved in a lot equipment projects in the field of marine.

JIAN WANG (Member, IEEE) was born in Anhui, China, in 1981. He received the B.S. degree in mathematics and the M.S. degree in electronic engineering from Anhui University, Hefei, China, in 2004 and 2007, respectively, and the Ph.D. degree in electronic engineering from Shanghai Jiao Tong University, Shanghai, China, in 2012.

He is currently serves as a Professor with the Faculty of Electrical Engineering and Computer Science, Ningbo University, Ningbo, China. His current research interests include computational electromagnetics, electromagnetic compatibility, electromagnetic protection of communication systems, signal integrity analysis and design of high-speed circuits, and microwave circuit design.

DONGYAN ZHAO (Member, IEEE) received the B.S. and M.S. degrees in mechanical engineering from Shanghai Jiao Tong University, Shanghai, China, in 1992 and 1998, respectively. After ten years at the State Grid Key Laboratory of Power Industrial Chip Design and Analysis Technology, she was appointed as the Director of the Chip Key Laboratory of Beijing Smart Chip Microelectronics Technology Company, Ltd. She has been an Adjunct Researcher with the Micro-Nano Electronics Department, Zhejiang University. Her research interests include antenna design, chip reliability design, and electromagnetic compatibility.

WEN-YAN YIN (Fellow, IEEE) received the M.S. degree in electromagnetic fields and microwave techniques from Xidian University, Xi'an, China, in 1989, and the Ph.D. degree in electrical engineering from Xi'an Jiao Tong University, Xi'an, in 1994.

From 1993 to 1996, he was an Associate Professor at the Department of Electronic Engineering, Northwestern Polytechnic University (NPU), Xi'an. From 1996 to 1998, he was the AvH Research Fellow at the Department of Electronic Engineering, Duisburg University, Germany. Since December 1998, he has been with the National University of Singapore (NUS), Singapore, as a Research Scientist. From April 2005 to December 2008, he was a Professor at the School of Electronic Information and Electrical Engineering, Shanghai Jiao Tong University (SJTU), Shanghai, China, where he is currently an Adjunct Ph.D. Candidate Supervisor with the Center for Microwave and RF Technologies. Since January 2009, he has been with the Zhejiang University (ZJU), Hangzhou, China, as a "Qiu Shi" Distinguished Professor. He is currently the Director of the College of Information Science and Electronic Engineering (ISEE), Innovative Institute of Electromagnetic Information and Electronic Integration (EIEI), ZJU. As a Leading author, he has published more than 260 international journal articles (more than 160 IEEE papers), including one international book and several book chapters. His main research interests include EMC and EM protection of communication platforms, computational electromagnetics and multiphysics and their applications, nanoelectronics, 3D IC, and advanced packaging.

Dr. Yin was an Editorial Board Member of *International Journal of RF and Microwave Computer-Aided Engineering*, from January 2012 to December 2014. He received the Science and Technology Progress Award of the First Class from the Local Shanghai Government of China, in 2005 and 2011, respectively; the National Technology Invention Award of the Second Class from the Chinese Government, in 2008; the Science and Technology Progress Award of the Second Class of China, in 2012; the Defense Technology Invention Award of the Second Class of China, in 2015; and several best paper awards of the international conference. He is the General Co-Chair of the 2017 IEEE Electrical Design of Advanced Packaging and Systems Symposium (IEEE EDAPS'2017), sponsored by the IEEE Electronic Packaging Committee. He was the Technical Chair of EDAPS in 2006 and 2011, respectively. From 2011 to 2012, he was an IEEE EMC Society as a Distinguished Lecturer. From January 2011 to December 2016, he was an Associate Editor of the *International Journal of Electronic Networks, Devices and Fields*. From January 2013 to December 2016, he was the IEEE EMC Society Chapter Chair. He is currently an Associate Editor for the IEEE TRANSACTIONS ON COMPONENTS, PACKAGING AND MANUFACTURING TECHNOLOGY; and the IEEE JOURNAL ON MULTISCALE AND MULTIPHYSICS COMPUTATIONAL TECHNIQUES.